

Probing the Stability of Thin-Shell Space Structures Under Bending

Fabien Royer^a, John W. Hutchinson^b, Sergio Pellegrino^{c,*}

^a*Graduate Aerospace Laboratories, California Institute of Technology,
1200 E California Blvd., Pasadena, CA 91125, USA*

*Currently at: Department of Aeronautics and Astronautics,
Massachusetts Institute of Technology, Cambridge MA 02139-4307, USA*

^b*John A. Paulson School of Engineering and Applied Sciences, Harvard University,
29 Oxford St, Cambridge, MA 02138, USA*

^c*Graduate Aerospace Laboratories, California Institute of Technology,
1200 E California Blvd., Pasadena, CA 91125, USA*

Abstract

The stability of lightweight space structures composed of longitudinal thin-shell elements connected transversely by thin rods is investigated, extending recent work on the stability of cylindrical and spherical shells. The role of localization in the buckling of these structures is investigated and early transitions into the post-buckling regime are unveiled using a probe that locally displaces the structure. Multiple probe locations are studied and the probe force versus probe displacement curves are analyzed and plotted to assess the structure's stability. The probing method enables the computation of the energy input needed to transition early into a post-buckling state, which is central to determining the critical buckling mechanism for the structure. A stability landscape is finally plotted for the critical buckling mechanism. It gives insight into the post-buckling stability of the structure and the exis-

*Corresponding author: sergiop@caltech.edu

tence of localized post-buckling states in the close vicinity of the fundamental equilibrium path.

Keywords: thin shells, buckling, stability, buckling localization, probing

1 **1. Introduction**

2 Thin-shell structures are used extensively in engineering applications. In
3 the aerospace sector, they are a key enabler of lightweight air and space
4 vehicles. While the use of thin-shell structures dramatically reduces the
5 structural mass, their mode of failure is often governed by buckling, which
6 is hard to predict. Buckling of thin-shell structures is characterized by a
7 sub-critical bifurcation, which means that the structure exhibits a falling
8 unstable post-buckling path right after the bifurcation point is reached. This
9 sudden drop in load-carrying capabilities leads to a dramatic collapse if the
10 post-buckling path never regains stability. Buckling is to be avoided at all
11 cost in these cases. However, in recent adaptive structures and materials,
12 buckling is no longer seen as failure but as a key shape-changing mechanism,
13 which enables switching among multiple functional configurations (Hu and
14 Burgueño, 2015; Medina et al., 2020). Whether buckling is used or to be
15 avoided, understanding its cause and predicting its occurrence is crucial, and
16 this has been the subject of numerous research studies over the past one
17 hundred years.

18 From the early 1920s, many shell buckling experiments were conducted,
19 and experimental buckling loads were consistently observed to be lower than
20 linearized classical buckling predictions. This discrepancy was later linked to
21 the presence of initial imperfections in the shell geometry (Von Karman and

22 Tsien, 1941; Donnell and Wan, 1950; Koiter, 1945). Indeed, for sub-critical
23 bifurcations, there exists a range of loading for which the structure’s fun-
24 damental (unbuckled) state is meta-stable, which makes the transition into
25 post-buckling extremely sensitive to imperfections and disturbances. On the
26 upside, this can also offer opportunities to build complex meta-stable struc-
27 tures (Zareei et al., 2020) by using buckled thin-shells as the main build-
28 ing blocks. In order to deal with the extremely sensitive buckling behav-
29 ior in engineering applications, the design process relies heavily on buckling
30 knockdown factors applied to the classical buckling load. Determining the
31 adequate knockdown factor, unique for each structure/load combination, is
32 of utter importance. It led to the NASA space vehicle design criteria for
33 the buckling of thin-walled circular cylinders (NASA, 1965). These crite-
34 ria, widely seen as very conservative, have been revisited by NASA’s Shell
35 Buckling Knockdown Factor (SBKF) Project, which has focused on testing
36 shells with known imperfections and non-uniformities in loading and bound-
37 ary conditions (Hilburger, 2012). It has been shown that knowing accurately
38 the structure’s initial geometry enables the accurate prediction of the buck-
39 ling event (Lee et al., 2016). However, in many applications, measuring the
40 shape of the structure before use can be both expensive and in some cases
41 impossible, and the traditional buckling and post-buckling predictions rely
42 on seeding a linear combination of the first buckling modes as imperfections
43 (Riks, 1979; Rahman and Jansen, 2010).

44 Another complication arising from unstable bifurcations is the localiza-
45 tion of buckling deformations. This is observed for instance for beams on an
46 elastic foundation (Wadee et al., 1997) and more importantly for thin-shell

47 structures such as the compressed cylindrical shell (Hunt and Neto, 1991) as
48 well as the spherical shell under pressure (Hutchinson, 2016). The nature of
49 localization itself generates a large number of post-buckling solutions even
50 for a small set of classical buckling modes, since the deformations can localize
51 at many different locations on the structure. This is referred to as spatial
52 chaos (Thompson and Virgin, 1988). Localization can arise on post-buckling
53 branches determined by the buckling modes, as observed in the spherical shell
54 under pressure (Audoly and Hutchinson, 2020; Hutchinson and Thompson,
55 2017). In addition, localization can also appear on post-buckling paths dis-
56 connected from the fundamental path while running asymptotically close to
57 it (Groh and Pirrera, 2019). In both cases, localized buckling can be trig-
58 gered earlier than the first buckling load if a small amount of energy is input
59 into the structure. It has been shown, for the compressed cylindrical shell,
60 that a single localized dimple forming in the middle of the structure consti-
61 tutes the lowest escape into buckling (Horák et al., 2006) and may therefore
62 be the critical buckling mechanism. This mode is not a bifurcation per se,
63 but rather a mode "broken away" from the fundamental path. The single
64 dimple state sits on a ridge in the total energy of the system between the
65 pre-buckling well and the local post-buckling well and corresponds to the low-
66 est mountain pass between these two states in the energy landscape (Horák
67 et al., 2006). For the cylinder, the single dimple can evolve to more and more
68 complex post-buckling deformations through a series of destabilizations and
69 restabilizations, until the cylinder is fully populated by dimples (Kreilos and
70 Schneider, 2017; Groh and Pirrera, 2019). This process is called snaking and
71 adds additional complexity to the full post-buckling sequence resolution.

72 For all of the reasons mentioned above, predicting buckling is extremely
73 difficult for shell structures and often relies on a case by case approach.
74 Recent work has focused on the sensitivity of the buckling phenomenon to
75 disturbances in thin cylindrical and spherical shells. A non-destructive ex-
76 perimental method, first proposed in 2015 to study the meta-stability of
77 the fundamental path, focuses on determining the energy barrier separating
78 the fundamental path and critical localized post-buckling states (Thompson,
79 2015; Thompson and Sieber, 2016; Hutchinson and Thompson, 2017). The
80 search for the critical buckling mechanism is carried out by imposing a lo-
81 cal radial displacement in the middle of the structure using a probe. This
82 method effectively quantifies the resistance of a shell buckling in the single
83 dimple mode mentioned earlier. The method has been successfully applied
84 to cylindrical shells (Virot et al., 2017) and pressurized hemispherical shells
85 (Marthelot et al., 2017). These experiments quantified in particular the on-
86 set of meta-stability, often referred to as "shock sensitivity" (Thompson and
87 van der Heijden, 2014) and a comparison with historical test data has shown
88 that this specific loading can serve as an accurate lower bound for experi-
89 mental buckling loads (Groh and Pirrera, 2019; Gerasimidis et al., 2018).

90 More recent work has investigated the interaction between probing and
91 geometric defects in cylindrical (Yadav et al., 2021) and spherical shells (Ab-
92 basi et al., 2021). These experiments showed that a specific probing strategy,
93 called ridge tracking (Abramian et al., 2020), enables the non-destructive de-
94 termination of the actual buckling load of an imperfect shell. Probing in the
95 immediate vicinity of the dominant imperfection is required. Finally, a sim-
96 ilar probing methodology has been applied to circular arches (Shen et al.,

97 2021a), cylindrical shell roofs (Shen et al., 2021b), and prestressed stayed
98 columns (Shen et al., 2022), and the use of multiple probes has enabled the
99 exploration of the complete unstable behavior of these structures, beyond
100 limit and branching points.

101 The present paper applies these recent breakthroughs to more complex
102 thin-shell structures, and is inspired by recently proposed spacecraft struc-
103 tures that use thin-shell components to build large space systems. In partic-
104 ular, modular structural architectures for ultralight, coilable space structures
105 suitable for large, deployable, flat spacecraft (Goel et al., 2017; Arya et al.,
106 2016) are being investigated in the Space-based Solar Power Project (SSPP)
107 at Caltech. In the deployed configuration, each spacecraft measures up to
108 $60\text{ m} \times 60\text{ m}$ in size and is loaded by solar pressure. The main building
109 block is a ladder-type structure made of two triangular rollable and collapsi-
110 ble (TRAC) longerons (Murphey and Banik, 2011), connected transversely
111 by rods (battens). Scaled laboratory prototypes of this structure have been
112 built (Gdoutos et al., 2020, 2019), and analysis has shown that local buck-
113 ling plays a key role in its behavior (Royer and Pellegrino, 2020). The size
114 of the structure, together with the complexity of its components and the
115 distributed nature of the loading, would make it very challenging to conduct
116 experimental studies.

117 In order to address these limitations, a simpler structure is proposed in the
118 present paper and its behavior under pure bending is studied. This structure,
119 shown in Figure 1, is made of longerons and battens like the SSPP structures,
120 but the longeron’s complex original cross-section has been replaced by a
121 circular-arc cross-section. While this structure and loading are different from

122 the specific structures of interest for the above-described space application,
123 it enables us to draw general conclusions on the buckling of space structures
124 with thin-shell open cross-sections. The computational analysis presented
125 here investigates the buckling behavior of such a structure and assesses if and
126 when early transitions into post-buckling can occur, using the novel probing
127 methodology. It also serves as a proof of concept for the experimental study
128 in Royer (2021).

129 The paper is structured as follows. Section 2 describes in more detail the
130 structure and the problem. Following a classical buckling analysis, Section 3
131 highlights the importance of localization and spatial chaos and justifies the
132 use of the newly-introduced probing methodology. In Section 4, probing is
133 applied along the entire structure to determine the location at which local
134 buckling can appear, and a critical probing scheme is identified. The analysis
135 is then generalized in Section 5 to more complex probing scenarios exhibit-
136 ing instabilities, and leads to an energy map from which the critical buckling
137 mechanism is identified. Finally a stability landscape of shell buckling is
138 computed in Section 6 to highlight key characteristics of the critical buckling
139 mechanism. It shows qualitative agreement with landscapes previously con-
140 structed for cylindrical and spherical shells, and for ladder-type structures
141 containing TRAC longerons (Royer and Pellegrino, 2020, 2022).

142 **2. Computational model of strip structure**

143 *2.1. Geometry and material properties*

144 The analysis presented in this paper is restricted to the single geometry
145 shown in Figure 1. The dimensions were chosen on the basis of a future

146 experiment that will use an existing experimental apparatus.

147 The structure, referred as a strip, is composed of two thin-shell longerons
148 of length 0.4 m and with circular-arc cross section. The opening angle is
149 60 deg, the arc radius is 10 mm, and the shell thickness is 0.1 mm, which
150 correspond to a bending stiffness comparable to the SSPP structures. The
151 two longerons are connected by six regularly spaced transverse circular rods
152 called battens. The batten spacing is 80 mm, which ensures that several
153 battens connecting the two longerons. The batten length is 50 mm, and the
154 batten cross-section radius is 1 mm.

155 A finite element model of the structure is built using the Abaqus 2019
156 commercial software. The longerons are modeled with 4-node reduced inte-
157 gration shell elements (S4R) and the battens with linear 3D beam elements
158 (B31). An isotropic material with Young's modulus $E = 130$ GPa, and
159 Poisson's ratio $\nu = 0.35$ is considered for both battens and longerons.

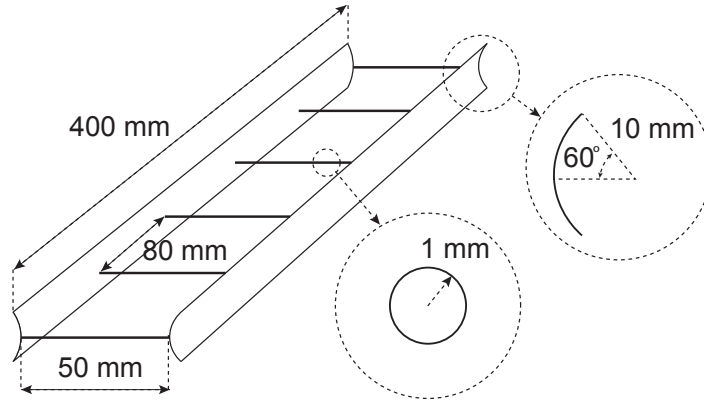


Figure 1: Strip structure composed of two thin-shell longerons connected by battens.

160 *2.2. Finite element analysis*

161 The end battens and the longeron end cross-sections are made unde-
162 formable and fully coupled to reference points R1 and R2, as shown in Figure
163 2. The boundary conditions and loading are applied to these reference points.
164 The structure is simply supported at both ends: one reference point is pinned
165 (all translations blocked) at one end while the z -translation is allowed for the
166 reference point at the other end. Two equal and opposite moments of mag-
167 nitude M are applied at the reference points, and an arc-length solver (Riks
168 solver in Abaqus standard) is used to statically deform the structure and ex-
169 tract the overall moment/rotation curve. In addition, in Section 4, for each
170 value of the moment, the top edge of the longeron will be probed by apply-
171 ing a transverse nodal displacement U_x at location z , and the probe reaction
172 force will be extracted. The two control parameters in these calculations are
173 thus the end moment and the probe displacement.

174 This strip structure has nonlinear pre-buckling behavior, meaning that
175 the computed buckling eigenmodes change as the structure approaches the
176 buckling limit. This type of nonlinearity was previously reported for thin
177 shell structures (Leclerc and Pellegrino, 2020). Hence, we will need to distin-
178 guish between two types of bifurcation buckling analyses and their associated
179 modes. We will use the standard terminology, classical buckling loads and
180 modes, for results in which the pre-buckling state used in the eigenvalue
181 analysis has been linearized, either about the condition at zero load or at
182 a non-zero load. Our approach will be making use of these eigenloads and
183 eigenmodes to gain insight into the buckling behavior of the strip. How-
184 ever, most references to buckling load and modes throughout the paper will

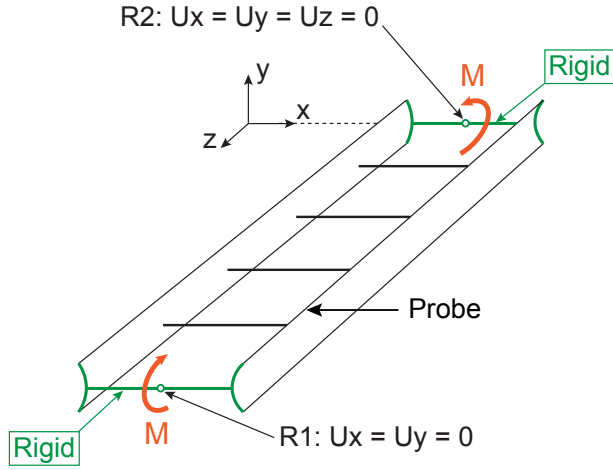


Figure 2: Schematic representation of finite element model. The end battens and cross-sections (green) are undeformable. R1 is allowed to translate along the z -axis and to rotate along all 3 axes, R2 is pinned and is free to rotate. Two equal and opposite moments are applied at the reference points. For a probing simulation (Section 4), a probe is applied to the top edge of the longeron (longeron and z location determined by probing scheme). It consists in an applied displacement on the probe node directed along the x -axis.

185 be to "exact" buckling loads and modes computed by analyzing the bifur-
 186 cation from the nonlinear pre-buckling state. We will mostly refer to the
 187 "exact" analysis and its outcome with the brief terminology: buckling anal-
 188 ysis, buckling loads, and buckling modes. However, if there is any ambiguity
 189 the additional terminology, linearized or nonlinear pre-buckling state, will be
 190 appended.

191 3. Localization and spatial chaos

192 3.1. Buckling modes and limit points

193 The first step in assessing the buckling behavior of the strip is to carry
 194 out a classical eigenvalue analysis to determine a sequence of the applied mo-

195 ments and associated modes at which buckling bifurcations from the perfect
196 strip occur. This information gives a picture of not only the lowest buckling
197 load and associated mode but also of the bifurcation modes lurking above
198 the lowest critical mode. Such information gives insight into potentially im-
199 portant imperfection shapes and to "nearby paths" which might play a role
200 in the post-buckling behavior.

201 The computation of the "exact" bifurcation moments and modes is itself
202 an iterative procedure because the pre-buckling behavior is nonlinear. To
203 obtain first estimates of the bifurcation points, the pre-buckling nonlinearity
204 is neglected using the ground-state linearity to compute a sequence of the
205 lowest bifurcation eigenvalues (ABAQUS and other structural codes have op-
206 tions for making such eigenvalue evaluations). These bifurcation estimates
207 are then used to guide the search for the bifurcations computed accounting
208 for nonlinear pre-buckling behavior. With the full pre-buckling nonlinearity
209 accounted for, the strip is then loaded by a moment below the first eigen-
210 value, the nonlinear pre-buckling problem is solved, and new estimates of the
211 sequence of bifurcation points are computed by linearizing about that state.
212 This iterative process is repeated with an increasing applied moment in each
213 iteration until the bifurcation moments converge. For the strip, nine bifur-
214 cation points are determined in the loading interval before the strip attains
215 a limit moment on the fundamental pre-buckling path. As noted earlier,
216 to distinguish between a buckling load of the perfect strip computed using
217 ground state linearity (traditionally called a "classical buckling load") and
218 the buckling load computed accounting for pre-buckling nonlinearity, we will
219 briefly refer to the latter as the "buckling load" and is associated eigenmode

220 as the "buckling mode". The results of this analysis are shown in Figure 3.

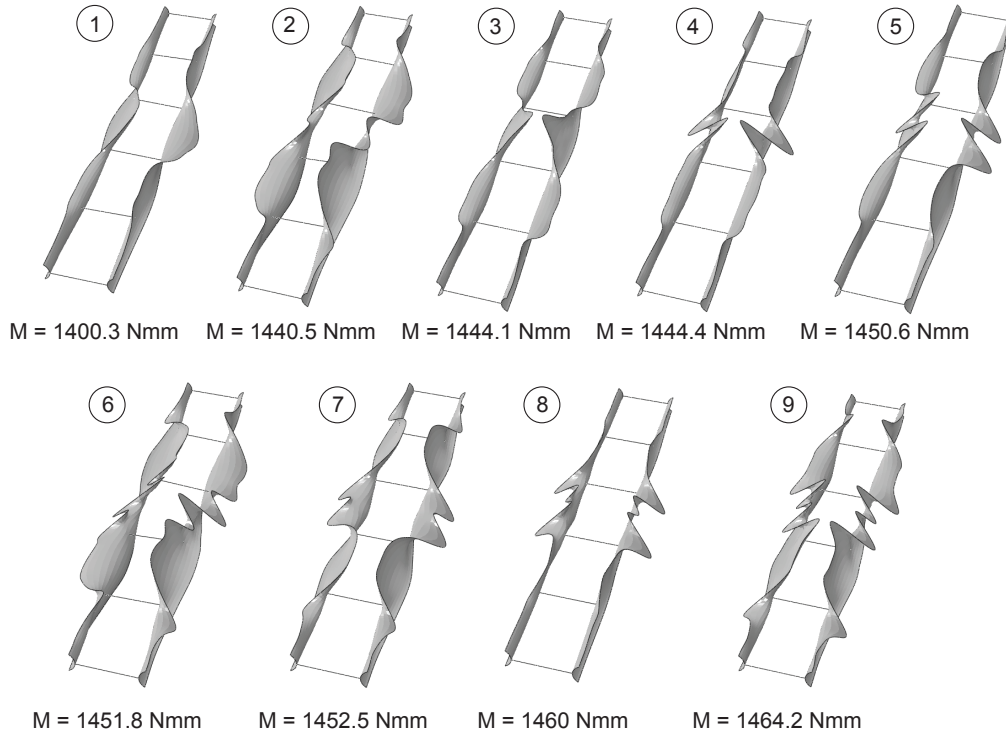


Figure 3: Nine buckling modes with associated buckling moments found on the strip fundamental path. For each mode, the deformations of both longerons are concentrated along the longerons' top edge (edge in compression). These deformations involve both inward (towards the strip center) and outward displacements. The battens do not exhibit any appreciable deformation.

221 Both a classical Newton-Raphson solver and the Riks solver are used to
222 trace the response of the structure in its unbuckled configuration. The Riks
223 method uses the load magnitude as an additional unknown and solves simul-
224 taneously for loads and displacements. The simulation progresses by incre-
225 menting the arc-length along the static equilibrium path in load-displacement
226 space, enabling the resolution of unstable responses. The Newton-Raphson

227 solver reaches a limit point at $M = 1,464.2$ Nmm, while the Riks solver
228 bifurcates from the fundamental path to a secondary branch at $M = 1,435$
229 Nmm. Note that this moment magnitude is between the first and second
230 buckling moments in Figure 3.

231 *3.2. Localization and post-buckling paths*

232 We wish to trace the post-buckling paths corresponding to several of
233 the lowest buckling eigenmoments and study the evolution of the structure's
234 shape along these paths. Of primary interest is the moment/rotation relation
235 for the strip when equal and opposite moments are applied at the strip ends
236 and the rotation corresponds to the rotation around the x -axis of the end
237 located at $z = 0$ (c.f., Figure 2).

238 As a first step, a standard method is used to trace the post-buckling paths
239 associated with the first three buckling modes as described next. Each mode
240 is seeded in the structure's initial geometry as a geometric imperfection. The
241 maximum amplitude of this initial imperfection is taken between 1% and 10%
242 of the shell thickness, t . The Riks solver is used to trace the post-buckling
243 response of the imperfect structure.

244 The computed paths are shown in Figure 4, and the corresponding de-
245 formed shapes are shown in Figure 5. For the second buckling mode, two
246 imperfection amplitudes have been used, yielding the two post-buckling paths
247 shown.

248 The main observation is that, contrary to the bifurcation buckling modes,
249 the deformed shapes for all the paths exhibit highly localized deformations.
250 For the first and second mode branches, the post-buckling shapes are quite
251 different from the initial imperfection. These shapes only exhibit inward

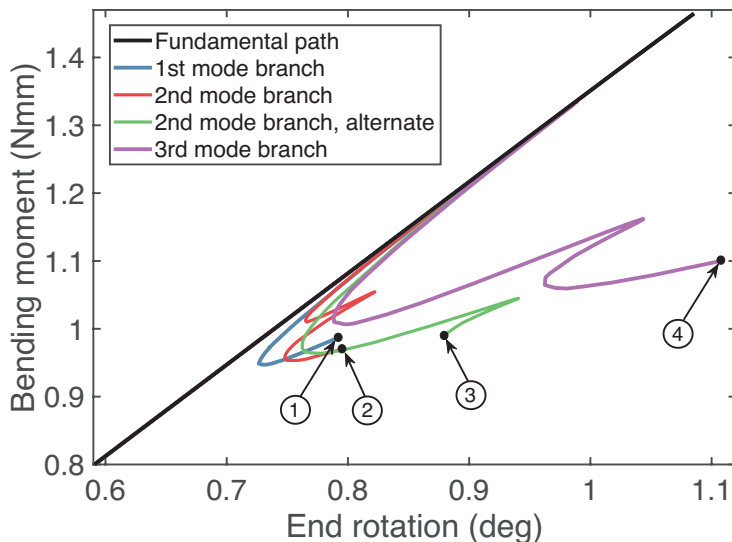


Figure 4: Moment vs. rotation curves for the strip. The fundamental path (black) stops at the limit point $M = 1,464.2$ Nmm. The first buckling mode branch (blue) is obtained by seeding the first mode as imperfection with an amplitude of $8\%t$. The second branch (red) is obtained for the second mode imperfection with an amplitude of $8\%t$. The alternate second branch (green) is obtained for the second mode imperfection with an amplitude of $10\%t$. The third branch (purple) is obtained for the third mode imperfection with an amplitude of $8\%t$.

252 buckling deformations, whereas the buckling modes also exhibit outward
 253 deformations. For the second mode branch, even a slight variation in im-
 254 perfection amplitude changes the buckling location. For the second mode
 255 and third mode, the post-buckling paths undergo destabilization and resta-
 256 bilization. This phenomenon is referred to as homoclinic snaking and is also
 257 observed in axially compressed cylindrical shells (Groh and Pirrera, 2019).
 258 It physically corresponds to the sequential formation of buckles leading to a
 259 fully buckled shell. Snaking may occur also in the remaining localized paths

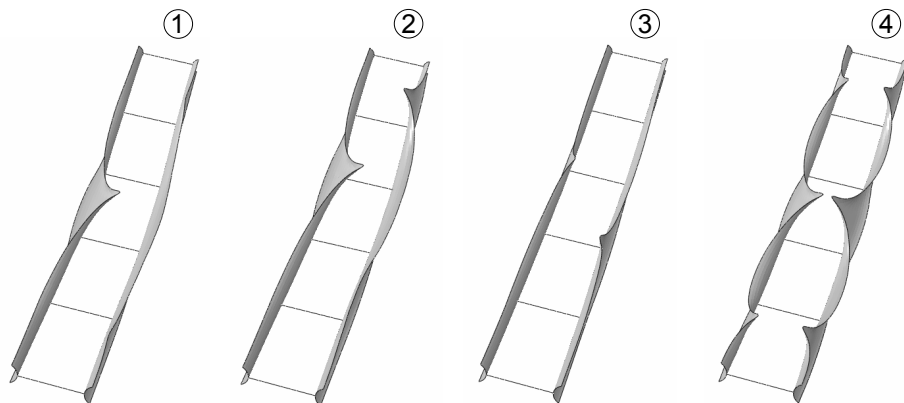


Figure 5: Deformed shapes with magnification of 15X, obtained at the end of the four post-buckling paths of Figure 4. They consist in localized longeron deformations and differ from the previously computed buckling modes. All deformations are inward, and the localization location differs between longerons for the mode 1 branch (labeled 1) and mode 2 branch (labeled 2).

260 if the analysis is pushed further. It is interesting to note that it was possible
 261 to resolve the post-buckling path for the third buckling mode without seeding
 262 any imperfection in the initial geometry.

263 For mode 1 and mode 2, the localization process initiates on the im-
 264 perfect structure's fundamental path, before reaching the falling unstable
 265 post-buckling path. The initial deformation grows proportionally to the ini-
 266 tial imperfection and then is followed by a transition to a localized mode
 267 shape before attaining a limit point. At this point, the location of maximum
 268 deformation has already been determined and, on the falling unstable path,
 269 the local deformation increases in amplitude without changing location. It is
 270 important to emphasize that the limit point for the imperfect structure is off-
 271 set from the perfect structure's fundamental path, although extremely close

272 to it, due to the eroding effect of the imperfection on the initial stiffness. In
273 addition, these limit points appear at values of applied moment lower than
274 the first buckling moment which reveals the structure's imperfection-sensitive
275 nature.

276 Figure 6 highlights the localization process for each of the first two buck-
277 ling modes. The displacement of the longeron top edge in the x - z plane is
278 plotted at the limit point, as well as at the first post-buckling restabilization
279 point and at the end of the post-buckling path. The normalized buckling
280 mode of the perfect strip is also reported as a dashed line, for comparison.

281 For mode 1, localization occurs on two levels. At the structure's scale,
282 local deformations only arise in longeron 1, while for longeron 2, the global
283 deformation tends to cancel the undulations associated with the initial im-
284 perfection away for the point of localization. At the longeron scale, the
285 deformed shape goes from a smooth hill to a sharp peak for longeron 2.

286 In addition, the localization process is not unique. Different localization
287 mechanisms are observed for buckling mode 2, depending on the imperfection
288 amplitude, as seen in the deformed shape comparison of Figure 5. The local-
289 ization of mode 2 for an imperfection amplitude of $8\%t$ is shown in Figure
290 6c-d. It highlights the sequential formation of the longeron 1 and longeron
291 2 buckle, characteristic of the snaking process. In the case of buckling mode
292 3, the buckling mode shape is relatively localized and resembles the shape
293 observed in Figure 5 for the two central buckles. Therefore, no further local-
294 ization is observed on the post-buckling path before the snaking process is
295 triggered, and four highly localized buckles are formed closer to the longeron
296 ends.

297 To conclude this section, we re-emphasize that multiple post-buckling
298 paths have been shown to have initially unstable behavior, and in some cases
299 the paths re-stabilized at lower loads. Four different imperfections based on
300 the first three buckling modes have been considered here; other imperfections
301 or linear combinations of buckling modes would give rise to different paths.
302 Seeding different imperfections has highlighted qualitatively the importance
303 of localization for this thin-shell structure and the fact its deformation can
304 easily localize at many different locations. This multiplicity of buckling and
305 post-buckling solutions is referred to as "spatial chaos." However, not all
306 possible localized paths have been considered, and hence it is not known
307 which path constitutes the easiest escape into post-buckling. Based on these
308 qualitative observations, the next section searches for the critical localized
309 path using the probing methodology introduced.

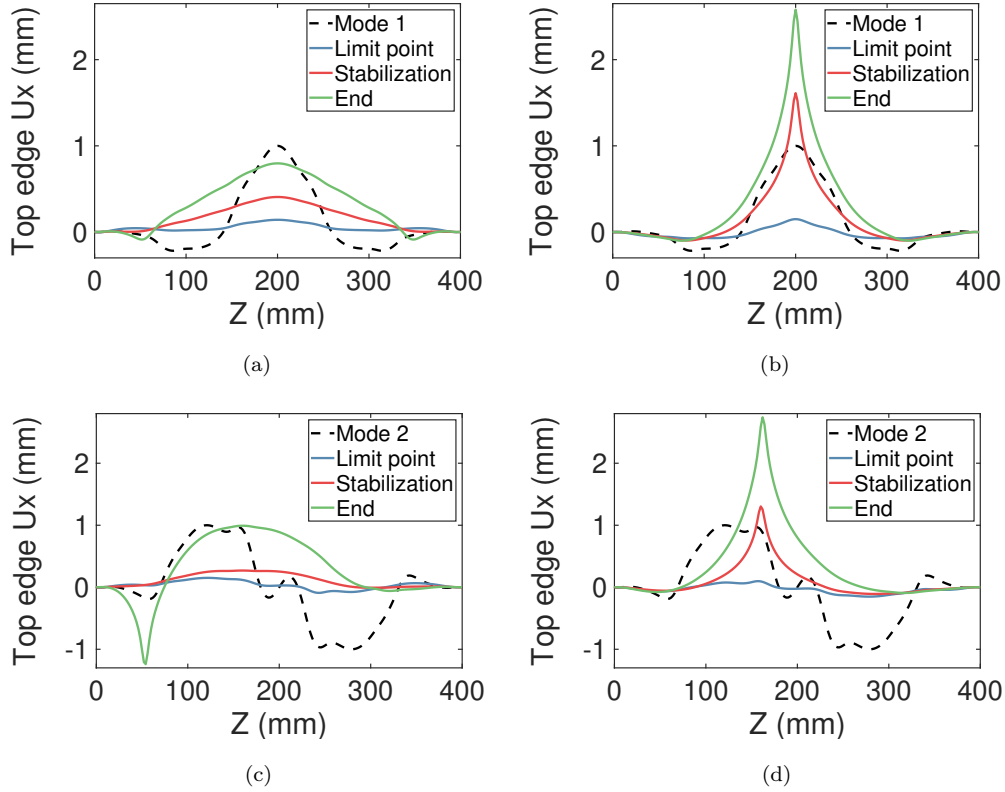


Figure 6: (a-b) Localization process for (a) longeron 1 and (b) longeron 2, on the first mode post-buckling path, for an imperfection amplitude of $8\%t$. The longeron top edge displacement in the x -direction is plotted as a function of the z location. The normalized buckling mode is shown as a dashed line. The evolution of the longeron top edge deformation is reported at the limit point, where the post-buckling path first stabilizes, and at the end of the post-buckling path. (c-d) Localization process on the second mode post-buckling path, for an imperfection amplitude of $8\%t$ for (c) longeron 1 and (d) longeron 2.

310 4. Probing along the strip length

311 4.1. Probing methodology

312 The previous section has shown that buckling localization can lead to a
313 large number of post-buckling paths. Hence, the focus in the rest of this
314 paper is on finding the critical buckling mechanism. Here "critical" means
315 finding the easiest way the structure can buckle or, in other words, finding
316 how early the transition into buckling can occur and which deformed shape
317 is most likely to arise.

318 Two situations may be encountered when end-moments are applied on
319 a strip. The first corresponds to an early transition to a path that inter-
320 sects the fundamental path, and for which the deformation matches one of
321 the buckling modes (at least at the bifurcation point). This situation may
322 arise for buckling mode 3, for which no imperfection is needed to resolve the
323 post-buckling path. The second situation corresponds to a transition to a
324 disconnected equilibrium path, running in close vicinity of the fundamental
325 path but without intersecting it (Hunt and Neto, 1991). In both cases, a finite
326 input of energy into the system is required to make the structure transition
327 early to a secondary equilibrium path. Note that here, "early transition"
328 means that the transition to post-buckling occurs before reaching the first
329 buckling moment. A key assumption made here is that the critical buckling
330 mechanism will exhibit highly localized deformations. This is generally the
331 case for thin-shell structures for which buckling is a sub-critical bifurcation
332 and is motivated by the observations made in the previous section.

333 The probing method, which uses a probe that displaces the structure
334 locally, is used to quantify the amount of disturbance needed to trigger early

335 localized buckling. In this paper, the probing method is explored numerically
336 and consists in applying a displacement directed along the x -axis to a node
337 on the top edge of the longeron (the probed node), as illustrated in Figure 2.
338 The top edge is chosen because it corresponds to the location of the largest
339 compressive stress when bending moments are applied to the structure.

340 The analysis goes as follows. Two end moments are applied on the perfect
341 structure. When the desired moment magnitude is reached, the moment is
342 kept constant and the probe displacement is increased. During probing, the
343 probe reaction force is computed. This process is repeated for a range of
344 moments, up to the first buckling moment, and for various probe locations
345 along the longeron's top edge. The Abaqus static general solver (Newton-
346 Raphson) is used for both the bending and probing steps. The analysis
347 presented in this section is restricted to probing paths for which the probe
348 displacement is monotonic.

349 Two features are of particular interest. The first corresponds to the range
350 of applied moments for which buckled equilibrium states exist. An equilib-
351 rium state is found when the probe reaction force falls to zero. When such
352 a situation is encountered, there exist at least two equilibrium configura-
353 tions for a given moment and therefore the fundamental path is meta-stable.
354 Above the moment for which negative probe forces are first encountered, a
355 disturbance may trigger early buckling. The second important feature is the
356 critical amount of energy that needs to be provided to the system to reach
357 the buckled equilibria. It indicates the level of disturbance needed for the
358 structure to transition early into these states.

359 Inspired by the types of deformations seen in the buckling modes, and

360 restricting the study to at most a single probe per longeron, five probing
 361 schemes have been investigated: double outward probing, double inward
 362 probing, alternate probing, single outward probing, and single inward prob-
 363 ing, as illustrated in Figure 7. These probing schemes were chosen such that
 364 it would be possible to trigger the localized buckling modes of Figure 5.

365 By characterizing the onset of meta-stability and the critical probe work
 366 needed to trigger buckling, we will be using probing as an efficient tool to
 367 navigate through the spatial chaos and to find the structure’s critical buckling
 368 mechanism.

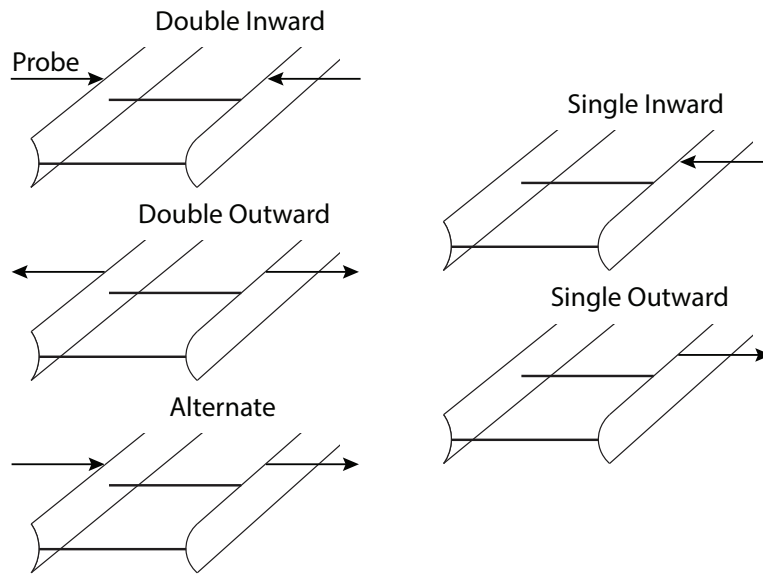


Figure 7: Five probing schemes considered in this paper, with arrows representing the transverse probe displacement.

369 *4.2. Double inward probing scheme*

370 The double inward probing scheme is considered first. In this case, con-
371 vergence is hard to achieve for probing with applied moments of around
372 $M = 1,100$ Nmm, because instabilities are encountered. These instabilities
373 are analyzed in detail in the next section.

374 For moments under 1,000 Nmm, the probing forces remain positive and
375 the contours of constant probe force exhibit local extrema in the probe lo-
376 cation / displacement plane. The probe force for two values of the moment
377 has been plotted in Figure 8 as a function of the probe location along the
378 longeron edge (z -axis) and of the probe displacement. Figure 8a shows the
379 probing map for $M = 800$ Nmm. The probe force is shown as a function of
380 the probe displacement along the x -axis (U_x) and the probe location along
381 the top of the longeron (x -axis). For ease of visualization, the regions cor-
382 responding to probe locations between 0 mm and 50 mm as well as between
383 350 mm and 400 mm are not shown since they exhibit large probe forces.
384 In these two regions, the probe force vs. probe displacement curve is almost
385 linear. For all other probe locations, the probe force increases monotonically
386 as the probe displacement increases. However, the map exhibits many
387 features, such as regularly spaced local minima of probe force for a given
388 probe displacement. The lowest local minimum is attained in the middle of
389 the structure (200 mm). The probe force is positive for all values of probe
390 displacement. Figure 8(b) shows the probing map for $M = 1,040$ Nmm.
391 For probe locations ranging from 0 mm to 60 mm and from 340 mm to 40
392 mm, the probe force increases monotonically as the probe displacement in-
393 creases. For all other probe locations, the probe force increases and then

394 decreases. Regularly spaced local minima of probe force appear, and nega-
 395 tive values are reached in the middle (200 mm). The spacing between local
 396 minima corresponds to the batten spacing.

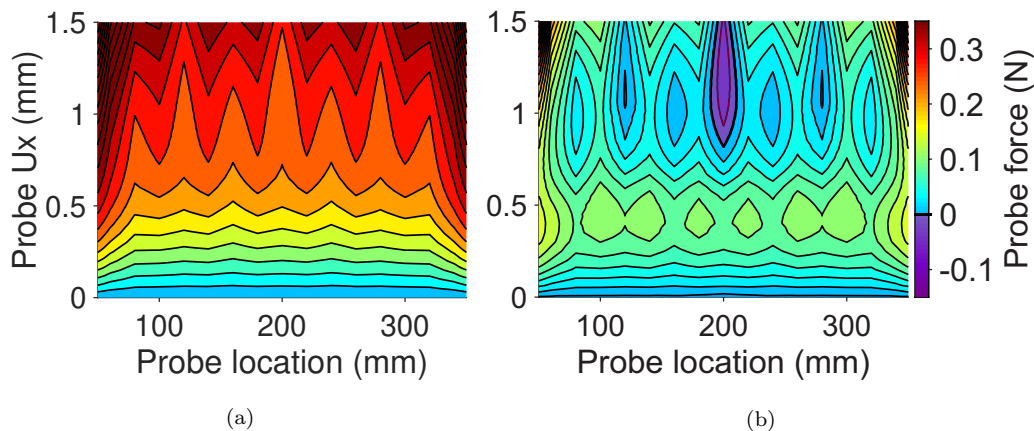


Figure 8: Double inward probing map for (a) $M = 800$ Nmm and (b) $M = 1,040$ Nmm. The spacing between contours is 0.05 N.

397 In fact, additional simulations showed that the probe force at the center
 398 first falls to zero for $M = 1,015.5$ Nmm. This critical load corresponds to
 399 the onset of meta-stability, at which early transition into buckling becomes
 400 possible. Based on the probing scheme, the associated post-buckling shape
 401 consists of an inward local buckle in the middle of each longeron. This shape
 402 resembles the third non-linear buckling mode found in Section 3.1.

403 4.3. Single inward probing scheme

404 The single inward probing scheme is considered next. The probing maps
 405 for four values of the applied moment are shown in Figure 9.

406 Figure 9a shows the probing map for $M = 800$ Nmm. As the probe
 407 displacement increases, the probe force increases monotonically, except near

408 the middle, where a basin of local minima appears (probe displacement of
409 1.2 mm). The probe force is positive everywhere.

410 Figure 9b shows the probing map for $M = 1,040$ Nmm. Local maxima
411 of probe force appear and form a hill separating the fundamental path from
412 regions with local minima. The local minima are negative near the middle of
413 the strip, whereas at other locations they are positive, although very close to
414 zero. This map resembles the map obtained for the double inward probing
415 scheme.

416 Figure 9c shows the probing map for $M = 1,200$ Nmm, which resembles
417 qualitatively Figure 9b. A local minimum of probe force appears for a probe
418 displacement of 0.2 mm, before reaching a second minimum at 0.35 mm, at
419 the center of a region of negative probe forces. However, when probing at
420 locations other than the middle, the probing path encounters instabilities as
421 the probe force decreases after the peak, and the Newton-Raphson solver
422 aborts. It leaves the probing map incomplete. The probe displacement for
423 which local minima of probe force are attained decreases as the moment
424 increases.

425 Figure 9d shows the probing map for $M = 1,350$ Nmm. The probe insta-
426 bilities appear as early as 0.1 mm of probe displacement and cause a severe
427 truncation of the map. The probing path for the mid-point of the structure
428 exhibits negative probe forces for displacements of 0.075 mm and 0.14 mm,
429 indicating the existence of two adjacent buckled equilibrium states. However,
430 the overarching goal of the probing method is to compute the minimum en-
431 ergy input needed to trigger early buckling for every probe locations, it is
432 not yet possible due to the probe instabilities. At the locations where the

433 probing sequence suddenly stops it is impossible to draw any conclusions
 434 regarding the structure's meta-stability. It is therefore necessary to resolve
 435 probing sequences past these instabilities, and this is the subject of Section
 436 5.

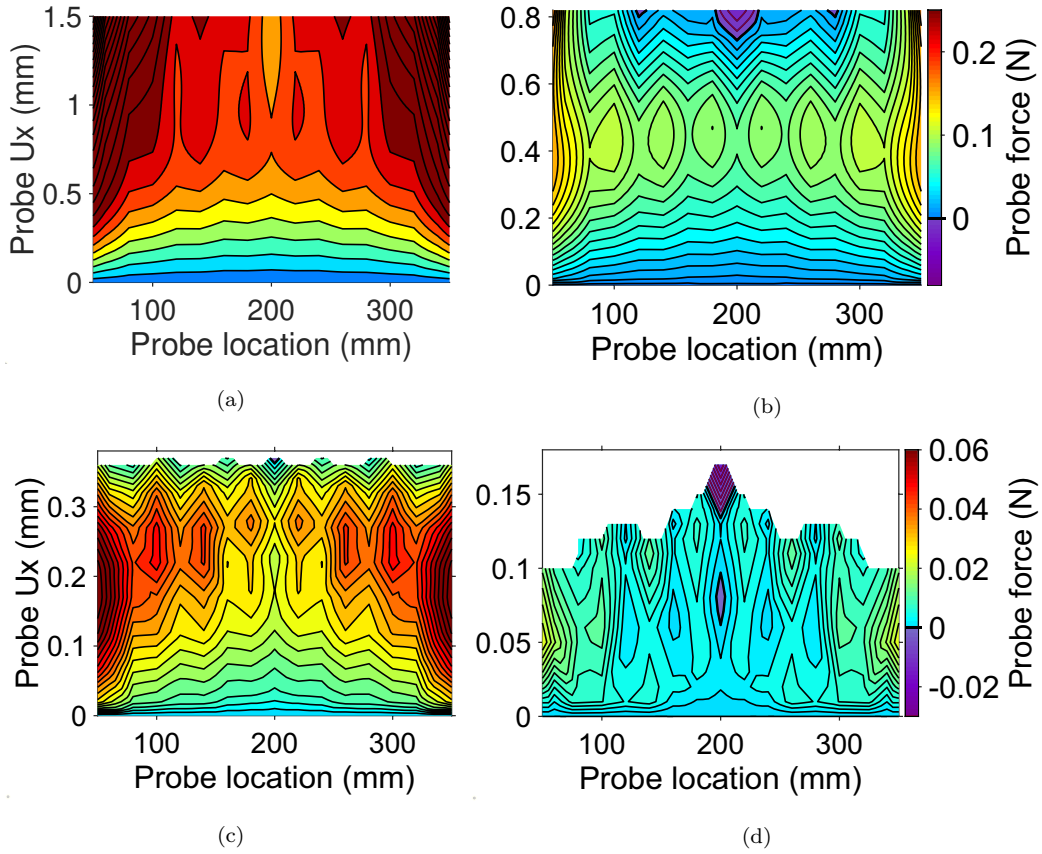


Figure 9: Single inward probing maps for (a) $M = 800$ Nmm, (b) $M = 1,040$, (c) $M = 1,200$ Nmm, and (d) $M = 1,350$ Nmm. The spacing between contours is 0.02 N for (a) and (b), and 0.005 N for (c) and (d).

437 An important observation is that meta-stability appears earlier for this
 438 type of probing than for the double inward probing scheme. For higher

439 moment magnitudes, the minimum of probe force is still achieved at the mid-
440 point of the structure, with regions of negative probe force spreading over a
441 larger portion of the structure. Therefore, there exist multiple locations at
442 which buckled equilibrium states are found. This supports the observations
443 of Section 3 where we saw that localization for the second mode imperfection
444 can occur at multiple locations. However, we see qualitatively that the hill
445 of probe force separating the unbuckled and buckled states is lowest at the
446 mid-point, which signifies that the minimum energy input required to form
447 an inward buckle is also achieved in the middle of each longeron.

448 *4.4. Outward and alternate probing schemes*

449 For the double outward probing scheme it is found that there is no value
450 of the moment for which the probe forces decreases to 0 N. Instead, as the
451 longeron is locally displaced outwards under constant applied moments, the
452 probe force always increases monotonically. Typically, the probe force reaches
453 1 N for a probe displacement of about 1 mm, which is an order of magnitude
454 higher than the probe force obtained with the double inward probing scheme.
455 Probing does not reveal any buckled equilibria in this case.

456 The alternate probing scheme involves an inward probe on longeron 1 and
457 an outward probe on longeron 2. The outward probe force increases monoton-
458 ically, as this case is similar to the double outward probing scheme. However
459 the inward probe force in the center becomes negative for all probe dis-
460 placements, above a certain moment magnitude. Although the disturbance
461 introduced by probing can be transferred between longerons, the outward
462 probe force never falls to 0 N and hence no buckled equilibria are found.

463 Similar behavior is observed for the single inward probing scheme. When

464 the outward probe displacement is increased, the probe force monotonically
465 increases, while an inward buckle forms in the unprobed longeron. Similarly
466 to the alternate probing scheme, no equilibrium configurations are encoun-
467 tered, but the probing path is truncated before the prescribed end displace-
468 ment is reached, due to instabilities. These instabilities are analyzed in
469 Section 5 and it is shown that buckled equilibria exist if probing is extended
470 past instabilities.

471 *4.5. Critical probe work and initial comparison of probing schemes*

472 In order to find the critical buckling mechanism for the strip structure,
473 the probing schemes presented above need to be compared. The critical
474 buckling mechanism corresponds to the minimum amount of energy needed
475 to reach buckled equilibria, but special care has to be taken when computing
476 the energy barrier to buckling and the critical probe work.

477 In previous buckling and probing studies, the energy barrier refers to
478 the difference in total potential energy between the unbuckled state and the
479 unstable buckled state. As explained in the introduction, the unstable buck-
480 led state corresponds to a saddle point (also called mountain pass point) in
481 the energy landscape and is attained for a critical value of the probe dis-
482 placement, when the zero threshold in probe force is reached. If the main
483 loading is kept constant, the probe work reaches a local maximum at this
484 critical displacement. We will use the terminology "critical probe work" to
485 refer to this local maximum of the probe work. When the probe displace-
486 ment is monotonic during probing (i.e., no folding of the path), and for
487 a displacement-controlled main loading, the critical probe work is equal to
488 the energy barrier. This scenario is for instance encountered for the probed

489 cylinder under constant end shortening (Viroc et al., 2017). However in the
490 present study, the energy barrier and the critical probe work can be different
491 for two reasons:

- 492 • Moment-controlled loading implies that probing occurs under a con-
493 stant value of the end-moment. During probing, the ends of the strip
494 rotate and hence the end-moments do work. As a result, the energy
495 barrier is greater than the critical probe work since it accounts for
496 the end-moments' additional contribution to the energy of the system.
497 However, the constant moments are part of the known conditions the
498 structure is subjected to during operation and, since the contribution
499 of an unknown disturbance is only represented by the probe, the quan-
500 tity of interest is the critical probe work. The study has been repeated
501 for a rotation-controlled loading and the results are presented in Ap-
502 pendix A. In the latter case, the probe work only contributes to the
503 total external work of the system.
- 504 • For unstable probing sequences, a vertical tangent can be reached, be-
505 yond which the probing path can fold. In such cases, snap-buckling
506 can be triggered before the zero probe force threshold is attained, and
507 the value of the critical probe work is computed at the point of vertical
508 tangent rather than at the first buckled equilibrium. Such cases are
509 presented and analyzed further in Section 5.

510 Next, the critical probe work for the two inward probing schemes is dis-
511 cussed. Since the probing path does not exhibit any instabilities in the middle
512 of the structure, for both schemes, the critical probe work required to reach

513 the buckled equilibrium states can be computed. The critical probe work
514 obtained for a central probe location and for both probing schemes is shown
515 in Figure 10.

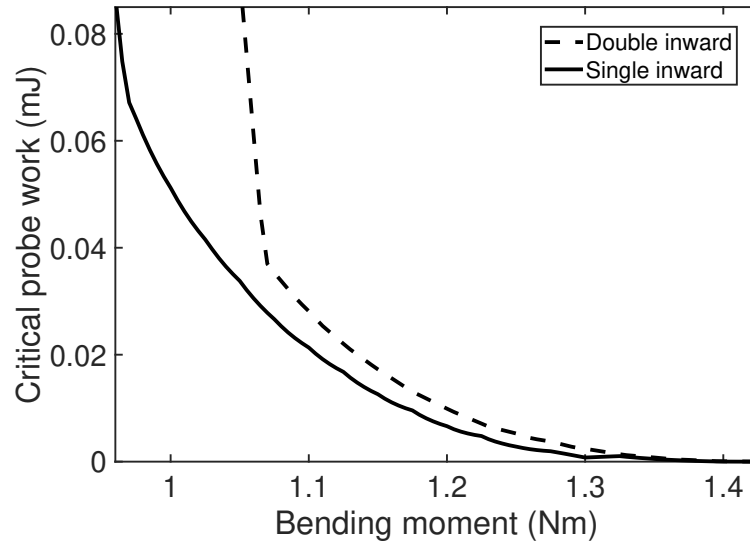


Figure 10: Critical probe work as a function of the applied bending moment, for both single and double inward probing schemes. It is smallest for the single inward probing scheme.

516 The single inward probing scheme gives a lower critical probe work than
517 the double inward probing scheme for the entire range of moments considered.
518 As a result, if buckling is triggered early, it will likely consist of a single
519 buckle in the middle of one of the longerons rather than in both longerons.
520 When comparing the local maximum of probe force obtained for both probing
521 schemes, we also see that it is lowest for the single inward probing scheme,
522 regardless of the probe location. It seems therefore that if meta-stability is
523 detected at a specific probe location, the single inward probing scheme would

524 also give the lowest critical probe work at this specific location.

525 Finally, it has been shown in this section that buckled equilibrium states
526 appear for lower values of moments for the single inward probing scheme. As
527 snaking appears to play a prominent role for this structure, we would expect a
528 sequential formation of single buckles which supports the energy comparison
529 between the two probing schemes. For all of these reasons, the rest of the
530 paper will focus only on the single inward / outward probing schemes.

531 **5. Unstable probing sequences**

532 *5.1. Single inward probing*

533 This section extends the probing simulations to cases in which instabil-
534 ities are encountered. The probing displacement is applied similarly to the
535 previous part of the study, but an arc-length solver (Riks solver) is now used,
536 which allows probing to continue after a vertical tangency (fold) in the probe
537 force vs. probe displacement plane has been reached. Additional probing
538 sequences are computed for the single inward probing scheme and for all
539 probing locations, and the two main types of path instabilities encountered
540 are analyzed.

541 The results of the analysis for a probe located at 100 mm from the end of
542 the structure are shown in Figure 11. For $M < 1,050$ Nmm, the probing path
543 is stable and the probe force exhibits a local maximum and local minimum.
544 However, the probe force is always positive and no locally buckled equilibrium
545 solutions exist. For $M = 1,050$ Nmm, a vertical tangent is encountered and
546 the path folds. The path eventually restabilizes for a value of probe force
547 of about -0.1 N. However, the restabilized path is short and does not reach

548 positive probe forces. This suggests that another bifurcation is encountered
 549 for a probe displacement of about 0.2 mm. This behavior is also encountered
 550 for higher values of moments, although the corresponding probing paths do
 551 not restabilize for positive values of probe displacement. Figure 12a shows
 552 the probing path for $M = 1,050$ Nmm with four points 1-4 marking key
 553 stages of the probing sequence.

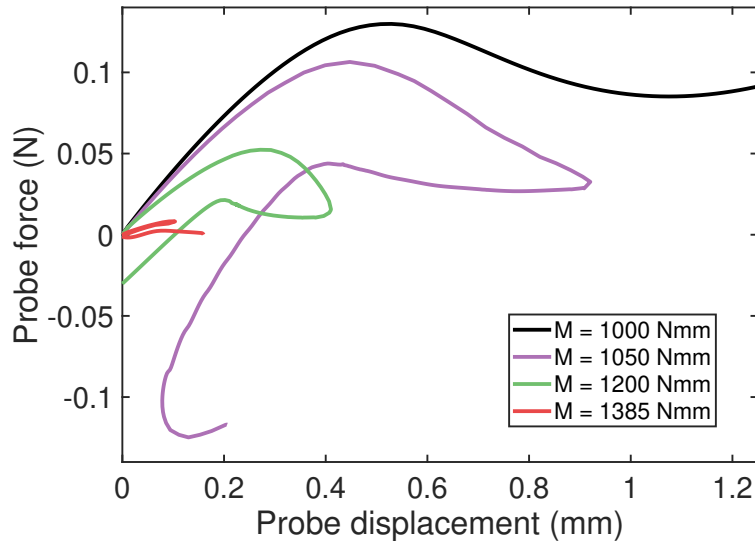


Figure 11: Probe force vs. probe displacement for a probe located at $z = 100$ mm and for four values of applied moment. The loop formed by the folded path becomes smaller as the moment magnitude increases until it folds on itself for $M = 1,385$ Nmm.

554 The deformed shapes corresponding to these four points are shown in Fig-
 555 ure 12b. On the stable part of the path (before reaching point 2), displacing
 556 the probe results in an increase of the local buckle amplitude. After point
 557 2, the probing path becomes unstable. As the probe displacement decreases,
 558 the probe force increases until it reaches point 3 and then decreases to 0 N at

559 point 4, which corresponds to a buckled equilibrium solution. This unstable
560 path corresponds to the change of location of the buckle formed during the
561 stable part of the path. At point 4, the structure is in a buckled equilib-
562 rium configuration, but the final buckle location does not correspond to the
563 probing location.

564 Note that the probe force vs. probe displacement curve has a positive
565 slope at point 4 which means that the equilibrium is stable. The critical
566 probe work required to reach the localized buckled configuration at point
567 4 corresponds to the shaded area in Figure 12a. It is important to point
568 out that this area does not correspond to the energy barrier, as explained
569 in Section 4.5. In order to compute the energy barrier, i.e. the difference in
570 total potential energy between the unbuckled state and the buckled state at
571 point 4, the area enclosed by the probing path would have to be considered.
572 The area under the curve formed by points 2, 3 and 4 would have to be
573 subtracted from the shaded area, and the work done by the end-moments
574 would have to be added.

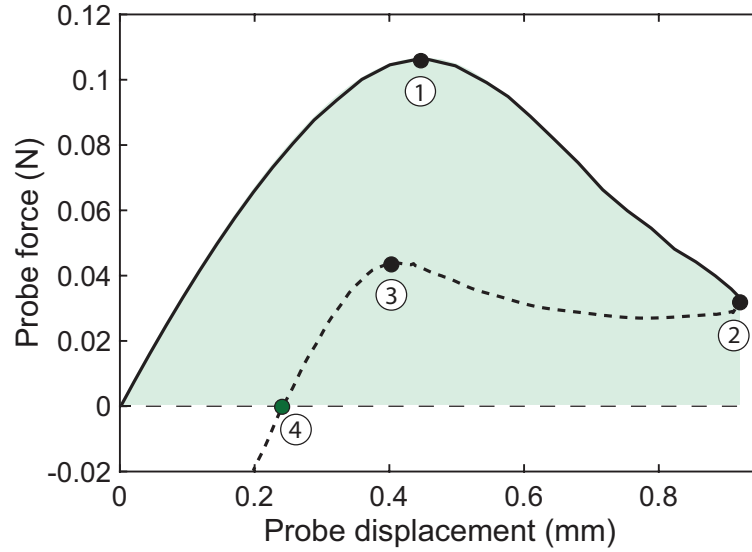
575 Path folding has also been encountered in compressed spherical shells
576 probed at the apex, under rigid volume control (Thompson and Sieber, 2016),
577 and all of the bifurcations that can arise and disrupt a probing sequence
578 have been described (Thompson et al., 2017). Two approaches have been
579 proposed to explore experimentally these unstable probing sequences. The
580 first one consists in introducing feedback control (Thompson et al., 2017).
581 If the probe displacement and probe force are chosen as inputs, it is then
582 possible to resolve vertical tangents. It is also possible to navigate around
583 the fold and avoid unstable probing paths by using the moment and probe

584 displacement as inputs. Another approach consists in using additional probes
585 to suppress instabilities (Thompson and Sieber, 2016).

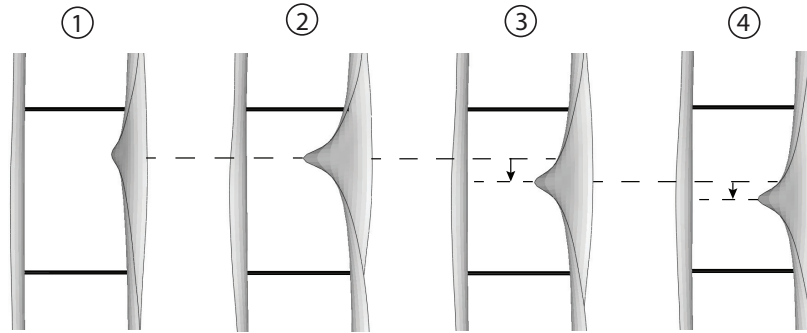
586 Next, the probing paths for a probe located at 160 mm from the end of the
587 structure are shown in Figure 13. For $M = 1,000$ Nmm, the path exhibits
588 a local maximum and a local minimum without reaching the zero threshold
589 for the probe force. The path is well behaved and can be resolved with
590 a Newton-Raphson solver. For $M = 1,050$ Nmm, the probe path reaches a
591 point of vertical tangency for a probe displacement 0.85 mm. The restabilized
592 path extends further and reaches positive probe forces, which indicates the
593 existence of a stable equilibrium solution.

594 As the moments increases in magnitude, the path folding is replaced by
595 path spiraling , which indicates that multiple equilibrium solutions exist. The
596 number of equilibrium solutions encountered on the probing path increases
597 as the moment increases. For $M = 1,200$ Nmm, four equilibrium solutions
598 are detected and for $M = 1,300$ Nmm the spiraling evolves to reveal five
599 equilibrium solutions. Close to the buckling load, at $M = 1,385$ Nmm, a
600 single path is observed for extremely small values of probe displacement,
601 which indicates an extremely low critical probe work.

602 The probing path for $M = 1,300$ Nmm is shown in Figure 14a, with four
603 equilibrium states labeled 1-5. The deformed shapes obtained at these points
604 are shown in Figure 14b. As the probe displacement increases, initially the
605 probe force increases and then decreases. The probing path becomes unstable
606 right before reaching the first equilibrium state (labeled 1). At this point,
607 a buckle in stable equilibrium (buckle 1) is formed in the longeron at the
608 probe location. The unstable path between states 1 and 2 exhibits negative



(a)



(b)

Figure 12: (a) Probe force vs. displacement for probe at $z = 100$ mm and $M = 1,050$ Nmm. Four key points are highlighted and correspond to the deformed shapes shown in (b). The solid and dashed lines correspond respectively to the stable and unstable probe characteristic under displacement control. The shaded area is the probe work needed to trigger snap-buckling. (b) Mode shapes obtained at points 1, 2, 3, and 4 on the probing sequence. The stable part of the path (point 1 and 2) corresponds to the growth of the buckle formed by the probe. On the unstable part of the path (points 3 and 4), the previously formed buckle shifts location. Deformations have been magnified by a factor 20.

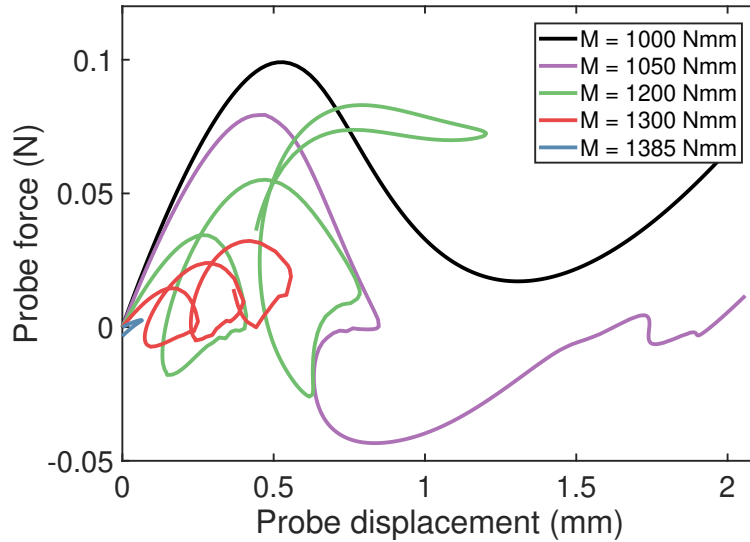
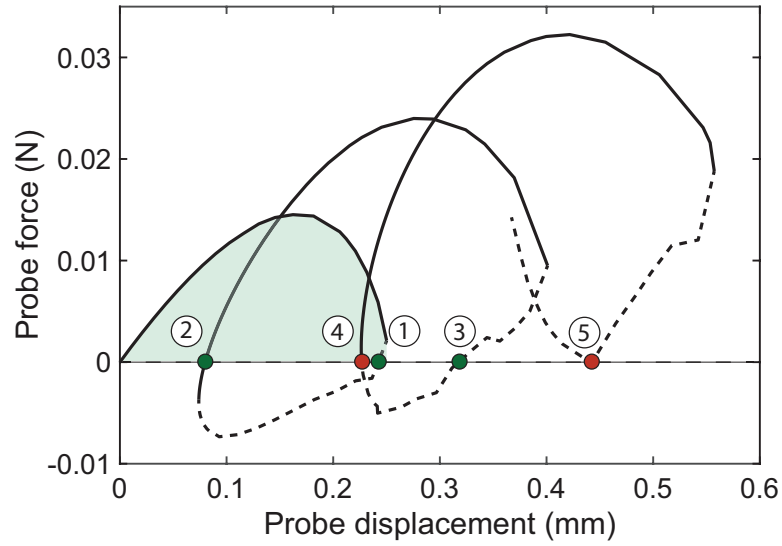


Figure 13: Probe force vs. displacement for probe at 160 mm and for five values of applied moment.

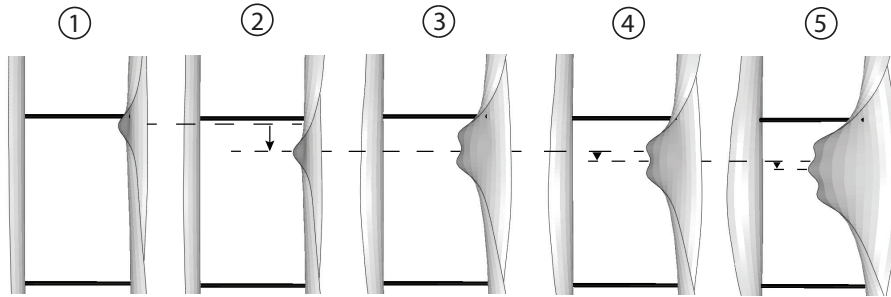
609 probe forces, and the initially formed buckle travels along the longeron's
 610 top edge. This situation is similar to the 100 mm probe location, but the
 611 main difference is that the path restabilizes with a sudden increase in probe
 612 force. Point 2 is now also an equilibrium state, whereas previously only one
 613 equilibrium solution was found. Equilibrium state 2 is also stable. From state
 614 2 to state 3, the probe force increases, and the magnitude of the maximum
 615 probe force is about twice the one attained before state 1. On this part of the
 616 path, buckle 1 continues to travel along the longeron, and a second buckle
 617 (buckle 2) forms at the probe location. The path loses stability at a probe
 618 displacement of about 0.4 mm and reaches the stable equilibrium 3, for which
 619 buckle 1 and buckle 2 are sustained, forming a "train" of 2 buckles. This
 620 buckle formation shifts location before reaching the unstable equilibrium 4.

621 The path proceeds with a third loop and the 2-buckle formation continues
622 traveling, while a third buckle (buckle 3) is formed at the probe location.
623 The path reaches equilibrium 5 for which 3 buckles in series are sustained
624 in the longeron. Note that point 5 also corresponds to a local minimum of
625 probe force and as a result, no more negative probe forces appear on the
626 path.

627 Two other interesting behaviors are observed. First, closer to the strip
628 ends (probe location between 20 mm and 60 mm) some hysteresis is found.
629 The probe displacement and probe force first increase, until reaching a limit
630 point, after which the probe displacement decreases and the path returns
631 to the origin. However, the return path lies below the original, stable path,
632 indicating lower probe forces. Physically, this indicates an interaction be-
633 tween the longerons: the inward displacement imposed on longeron 1 by the
634 probe causes a macroscopic in-plane bending of the full structure, causing
635 the unprobed longeron (longeron 2) to buckle. A similar transfer of distur-
636 bance between longerons, through the battens, was also encountered for the
637 alternate probing scheme. Secondly, for some combination of probe locations
638 and moments, the solver stops before the end of the analysis and the full
639 probing path cannot be resolved. This is due to the presence of secondary
640 bifurcations, and therefore the loss of a unique equilibrium path. While path
641 folding and spiraling could be resolved using the Riks solver alone, continuing
642 these probing paths after the bifurcation would require an imperfection to be
643 added in the initial geometry, or more sophisticated continuation algorithms
644 (Groh et al., 2018), which is beyond the scope of this paper. In most cases,
645 path folding is observed before reaching the bifurcation point, but the path



(a)



(b)

Figure 14: (a) Probe force vs. displacement for a probe located at $z = 160$ mm and for a moment of $M = 1,300$ Nmm. The five points highlighted correspond to the deformed shapes shown in (b), magnified by a factor of 40. The solid and dashed lines correspond respectively to the stable and unstable probe characteristic under displacement control. The stable and unstable equilibrium configurations are indicated by green and red dots, respectively.

646 stops before reaching the zero threshold for the probe force. Therefore, no
647 equilibrium solutions can be detected. However, it is still possible to compute
648 the probe work required to trigger snap-buckling, when the vertical tangent
649 is reached.

650 *5.2. Single outward probing*

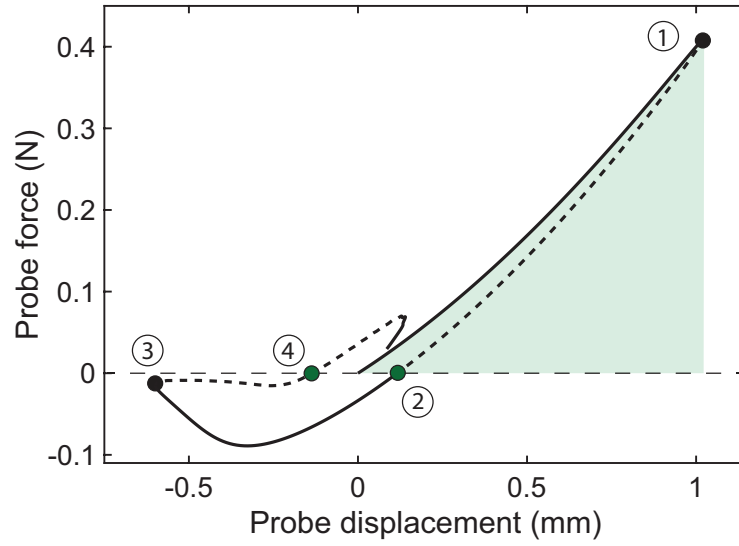
651 No buckled equilibrium solutions were detected when the single outward
652 probing scheme was used in Section 4, and the probe force increased monoton-
653 ically as the probe displacement increased. Even if buckled equilibrium states
654 seemed unlikely for this type of probing, the probing paths had been prema-
655 turely terminated by instabilities and therefore no final conclusion could be
656 reached regarding their existence. Here, the Riks solver is used to compute
657 the probing paths past vertical tangents. Surprisingly, it was found that the
658 single outward probing scheme is able to trigger inward buckled equilibria,
659 and the two main buckling mechanisms are analyzed below.

660 The first buckling mechanism involves the formation of a buckle in the
661 unprobed longeron. Probing at a location $z = 180$ mm under a moment
662 of $M = 1,100$ Nmm triggers this behavior, and the corresponding probe
663 force vs. probe displacement curve is shown in Figure 15a. The structure's
664 deformed shapes obtained at selected points on the path are shown in Figure
665 15b. The probing sequence starts with a monotonic increase in probe force as
666 the probe on longeron 1 is displaced outwards. The deformed shape at point
667 1 shows the large displacement of the probed longeron but no localization is
668 observed. However pulling on longeron 1 results in a global in-plane bending
669 of the structure, which results in an inward displacement of the unprobed
670 longeron 2, since the two longerons are connected by the battens. Past point

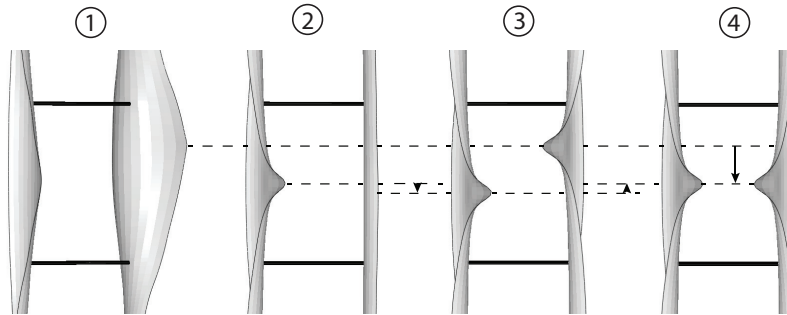
671 1, the probe displacement decreases and the inward displacement of longeron
672 2 localizes to form a buckle. At point 2, the inward buckle on the unprobed
673 longeron 2 is in equilibrium and stable. Once the probe displacement becomes
674 negative, the single inward probing scheme is recovered and an inward buckle
675 is formed on the probed longeron 1. Path folding is then observed which
676 physically corresponds to the buckle on longeron 1 moving along the longeron,
677 as described in the previous subsection. The only difference here is that the
678 initial outward probing results in an additional inward buckle on longeron 2.

679 The second buckling mechanism is rather unexpected, as it corresponds to
680 the formation of an inward buckle in the longeron probed outwards. Probing
681 under a moment $M = 1,300$ Nmm and at a location of 120 mm leads to
682 this behavior. The corresponding probe force vs. probe displacement curve
683 is shown in Figure 16a and the structure's deformed shapes at key points of
684 the path are shown in Figure 16b. The probing sequence starts again with
685 a monotonic increase in probe force as the probe on longeron 1 is displaced
686 outwards. The deformed shape at point 1 shows the large displacement of
687 the probed longeron, but inward localization is observed farther away from
688 the probe, on the same longeron. Past point 1, the path becomes unstable
689 and the localized fold present at point 1 corresponds to an inward buckle on
690 the probed longeron. The local hump in probe force observed on the unstable
691 path corresponds to the buckle traveling until the stable equilibrium at point
692 2 is reached. After point 2, the single inward probing scheme is recovered
693 and an additional buckle is formed on the probed longeron. Path folding is
694 again observed in this case.

695 Finally, other types of outward probing paths are encountered for different

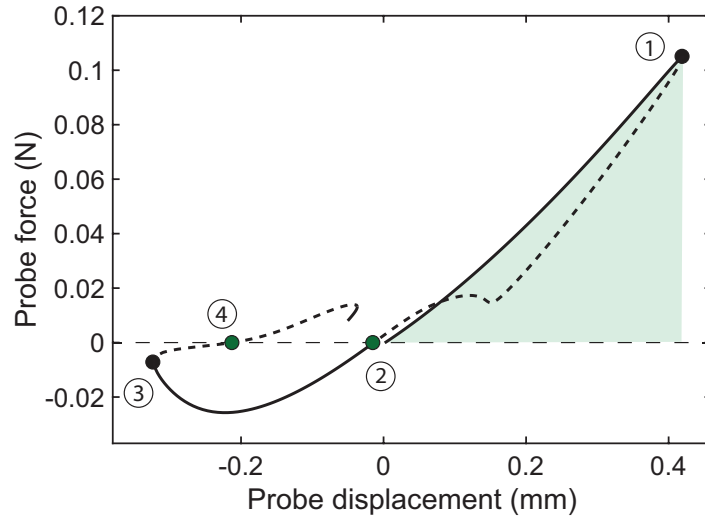


(a)

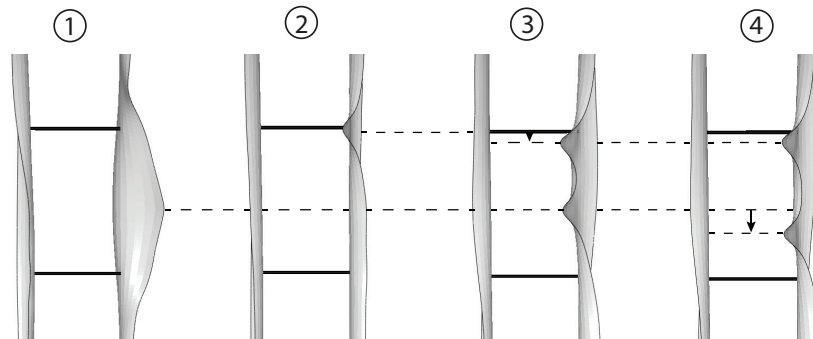


(b)

Figure 15: (a) Probe force vs. displacement for probe at $z = 180$ mm and $M = 1,100$ Nmm. (b) Deformed shapes corresponding to points 1, 2, 3, and 4, magnified by a factor of 30. The solid and dashed lines correspond respectively to the stable and unstable probe characteristic under displacement control. The stable equilibrium configurations are indicated by green dots.



(a)



(b)

Figure 16: (a) Probe force vs. displacement for probe at $z = 120$ mm and $M = 1,300$ Nmm. The four points highlighted correspond to the deformed shape shown in (b), magnified by a factor of 50. The solid and dashed lines correspond respectively to the stable and unstable probe characteristic under displacement control. The stable equilibrium configurations are indicated by green dots.

696 probe locations and consist of a superposition of the two simple buckling
697 sequences described above. Note that once the first buckle has been formed
698 by the outward probing scheme, these paths can exhibit spiraling and lead
699 to a complex series of buckles in equilibrium. An analysis of these complex
700 situations corresponding to even more equilibrium solutions is beyond the
701 scope of this paper.

702 The main take away is that both the single inward and single outward
703 probing schemes can trigger inward buckling, and no outward buckling has
704 been observed in either case.

705 *5.3. Critical probe work map*

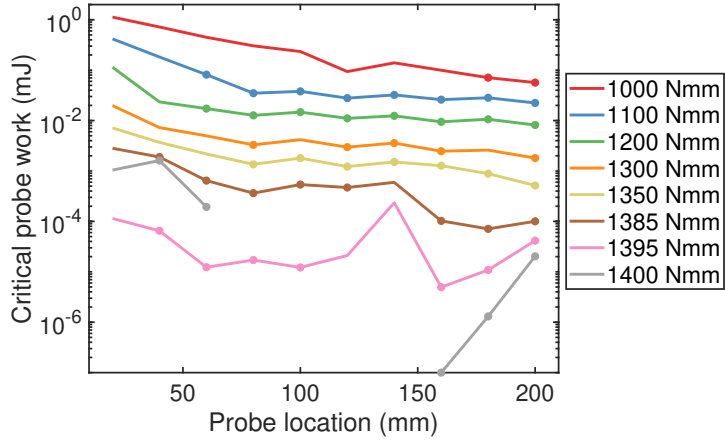
706 Repeating the analysis described above for all probe locations and mo-
707 ments, and for both the single inward and single outward probing schemes,
708 leads to the two critical probe work plots shown in Figure 17. Each color
709 corresponds to a specific moment magnitude. Dots denote the first zero
710 threshold in probe force, corresponding to a buckled equilibrium. In some
711 cases, secondary bifurcations are encountered on the probing path before
712 reaching the zero probe force threshold. In this case, additional techniques
713 would need to be used to trace the full probing path, however, the critical
714 probe work has been computed and reported without a dot. If the probing
715 path can be fully resolved but never crosses the zero probe force threshold,
716 the maximum work done by the probe is also reported without a dot. Since
717 the problem is symmetric with respect to the middle transverse axis of the
718 strip, only results for half a strip have been presented in Figure 17. No early
719 buckling can be triggered for probes between $z = 0$ mm and $z = 20$ mm, and
720 hence this region is not shown. Finally, it is important to highlight that the

721 probe location does not necessarily coincide with the buckling location.

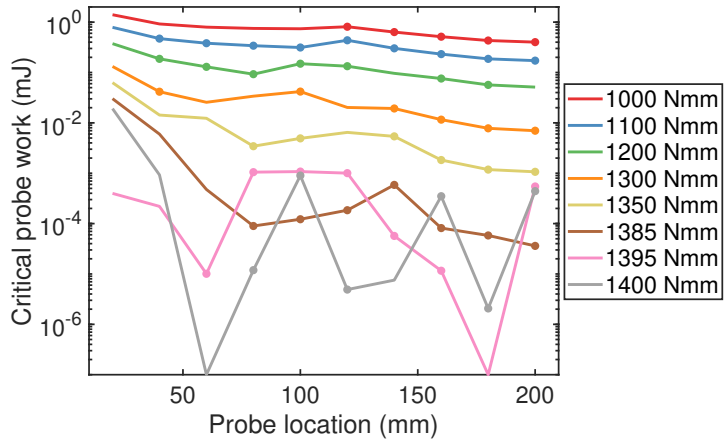
722 The critical probe work for the inward probing scheme is shown in Figure
723 17a. Multi-stability is first detected for probing at the mid-point and for $M =$
724 950 Nmm. For higher values of the moment, the meta-stable region extends
725 to almost the entire length of the strip. For moments lower than 1,385 Nmm,
726 the minimum critical probe work is always reached for probing at 200 mm.
727 For $M = 1,000$ Nmm, it is about 0.06 mJ and drops to less than 10^{-3} mJ
728 for $M = 1,350$ Nmm. These magnitudes make early buckling extremely
729 likely to occur. Closer to the first buckling moment ($M = 1,400.3$ Nmm),
730 the location of the minimum critical probe work changes. It is attained for
731 a probe at 180 mm for $M = 1,385$ Nmm and shifts to 160 mm for higher
732 values of moments. Note that for this range of high moments, the critical
733 probe work drops to practically zero. At $M = 1,400$ Nmm, the critical probe
734 work first drops to effectively zero (marked as 10^{-7} in Figure 17).

735 The critical probe work for the single outward probing scheme is shown in
736 Figure 17b. Qualitatively, it resembles the single inward probing, however the
737 critical probe work is consistently higher for this type of probing, indicating
738 that inward probing is the critical disturbance for the strip structure. For
739 $M > 1,385$ Nmm, the minimum critical probe work is similar for inward
740 and outward probing. At $M = 1,400$ Nmm, the critical work first drops to
741 zero (marked as 10^{-7} in Figure 17) but for a probe location of 60 mm, which
742 differs from the single inward probing scheme.

743 For both probing schemes and for $M < 1,385$ Nmm (99% of the buckling
744 moment), the minimum critical probe work occurs for probing in the middle
745 of the structure and is extremely low. It can be concluded that early buckling



(a)



(b)

Figure 17: Critical probe work map for (a) single inward and (b) single outward probing scheme. Dots denote solutions corresponding to the first zero value of the probe force, corresponding to a buckled equilibrium. These plots show similar trends, except that the single outward probing scheme requires more energy to trigger inward buckles.

746 is most likely triggered by inward probing in the middle of the structure,
747 and it is thus the critical disturbance. For this specific case, the probing
748 and buckling locations are the same and, therefore, the critical buckling
749 mechanism consists of a localized single buckle in the middle of a longeron.

750 Finally, rotation-controlled simulations have also been carried out. The
751 corresponding critical probe work maps are presented in Appendix A.

752 **6. Stability landscape for critical localized buckling**

753 The notion of a stability landscape of shell buckling was introduced (Viro
754 et al., 2017) as a way to characterize the meta-stable nature of cylindrical
755 thin-shell buckling. The experiments in this original study used soda cans,
756 and a local radial displacement was imposed in the middle of the compressed
757 can using a small ball probe (called a "poker" in Viro et al. (2017)).

758 The stability landscape is the surface created when the probe force is
759 plotted as a function of the probe displacement for various levels of the main
760 loading parameter (axial compression or end-shortening of the cylinder). The
761 landscape provides a very useful way to quantify the impact of probing on
762 the buckling behavior and a general way to study the structure's buckling
763 sensitivity to disturbances. In the cylinder case, the probe location coincides
764 with the location of the critical buckling mechanism, which corresponds to
765 the formation of a single dimple in the middle of the cylinder. Hence, in this
766 case the probing experiment is aimed at triggering this specific mode (lowest
767 mountain pass point).

768 In the previous section, the critical buckling mechanism for the strip
769 structure was identified. It was established that local buckling can first ap-

770 pear as a single inward buckle forming in the middle of one longeron. As a
 771 result the critical stability landscape of shell buckling for this new structure
 772 has been constructed and is presented in Figure 18.

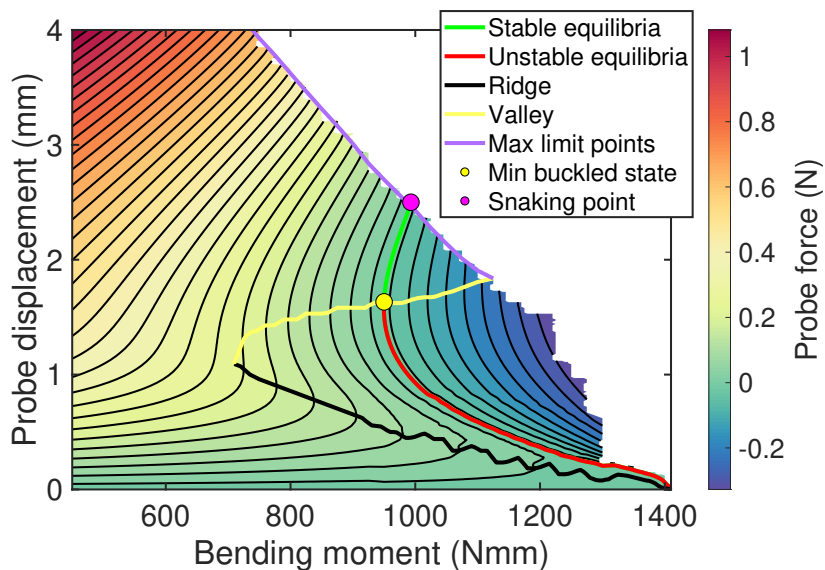


Figure 18: Stability landscape for the strip critical buckling mechanism (single inward buckling in the middle), showing a region of negative probe force enclosed by a stable/unstable buckled equilibrium contour, separated from the fundamental path by a ridge of probe force. No buckles can be sustained in the structure for moments below the minimal buckling moment ($M = 950$ Nmm).

773 This landscape matches qualitatively the landscape for the compressed
 774 cylindrical shell, as well as the stability landscape for more structural complex geometries and loading (Royer and Pellegrino, 2020). Several important
 775 features are observed (Viroto et al., 2017) and are explained here. The point
 776 of spontaneous buckling corresponds to the state for which the structure
 777 will undergo buckling without any action from the probe. This point is
 778 reached when the moment attains the buckling load (accounting for nonlin-
 779

780 ear pre-buckling deformation). However, before reaching this point, buckled
781 equilibrium solutions are accessible through probing. These solutions corre-
782 spond to the contour for which the probe force is zero (for a non-zero probe
783 displacement). It consists of two parts: stable and unstable. For a specific
784 value of the moment, corresponding to the lowest value of moment for which
785 a buckled equilibrium solution exists, the stable and unstable states coincide.
786 This condition represents the onset of meta-stability and the associated state
787 is called the minimally buckled state (Virot et al., 2017). This moment value
788 is denoted as the minimal buckling moment.

789 For the strip structure, the minimal buckling moment is 950 Nmm (68% of
790 the buckling moment), and the probe displacement at the minimally buckled
791 state is 1.6 mm. Below the minimal buckling moment, no local buckles can
792 be sustained in the structure. This load may serve as an effective lower bound
793 for experimental buckling loads (Groh and Pirrera, 2019).

794 During a moment-controlled experimental probing sequence, where the
795 probe is not attached to the structure, the longeron flange will dynamically
796 snap as soon as the probe reaches past the unstable equilibrium contour, since
797 the probe will experience negative reaction forces. Depending on the moment
798 at which probing is carried out, the structure can restabilize and reach the
799 stable equilibrium contour. For a moment above a critical value, correspond-
800 ing to the snaking point of Figure 18, the structure will not restabilize and
801 may completely collapse. The snaking moment is $M = 993$ Nmm (71% of
802 the buckling moment). It is possible to probe the stable post-buckling path
803 and compute the critical probe work required for early snaking, following the
804 same methodology.

805 It is important to realize that the existence of the stable equilibrium con-
806 tour is not guaranteed. It depends on the particular structure under study,
807 and also on whether the experiment/simulation is load controlled or displace-
808 ment controlled. For example, a spherical shell under external pressure will
809 exhibit stable buckled states when loaded under volume-control but has no
810 stable buckled states (other than complete collapse) under pressure-control
811 (Hutchinson and Thompson, 2017). For the SSPP strip structures described
812 in the Introduction, it has been observed that the stable buckled equilibrium
813 contour can extend much farther than the first buckling load (Royer and
814 Pellegrino, 2020).

815 The local maxima of probe force define the ridge of the stability landscape,
816 and form a hill of energy between the fundamental path and the unstable
817 buckled equilibrium states. At any applied moment, the critical probe work
818 is the minimum energy that must be input into the structure for it to locally
819 buckle. This quantity is directly related to the buckling sensitivity to distur-
820 bances, referred to as "shock-sensitivity" (Thompson and van der Heijden,
821 2014). The ridge meets the fundamental path at the point of spontaneous
822 buckling under prescribed probe force (but not under prescribed probe dis-
823 placement). Past this point, negative probe forces are encountered as soon
824 as the probe is displaced. The local minima of probe force form the valley
825 of the stability landscape, defining the limit beyond which probing paths
826 restabilize. The valley intersects with the buckled equilibrium contour at
827 the minimally buckled state after which the minimum probe force becomes
828 negative.

829 The ridge and valley intersect at $M = 710 \text{ Nmm}$ (51% of the non-linear

830 buckling moment), after which the landscape starts exhibiting a negative
831 probing stiffness. For higher values of probe displacements, the stability
832 landscape is bounded by limit points ending each probing sequence. The
833 ridge, valley, and maximum limit points form the landscape’s foldline which
834 defines more generally the range of stability for the structure against the sin-
835 gle buckle mode of deformation. Snaking, which corresponds to secondary
836 modes being triggered, will occur when the maximum limit points are ex-
837 ceeded.

838 Finally, rotation-controlled simulations have been carried out and yield
839 qualitatively the same landscape. The rotation-controlled stability landscape
840 is shown in Appendix A.

841 **7. Conclusion**

842 This paper has presented a numerical investigation of the buckling sen-
843 sitivity of a complex thin-shell strip structure, applying the novel probing
844 methodology previously used for cylindrical and spherical shells. The fo-
845 cus has been on a single geometry, inspired by novel designs for spacecraft
846 structures, with the goal of paving the way for experimental studies (Royer,
847 2021).

848 First, a classical post-buckling analysis has been conducted, which con-
849 sisted in seeding imperfections based on the structure’s buckling modes in the
850 initial geometry. This analysis has shown multiple localized post-buckling so-
851 lutions originating from a limited set of nine buckling modes, and providing
852 evidence that the structure exhibits spatial chaos.

853 The probing methodology is well suited to finding the critical buckling

854 mechanism. By probing along the entire structure, it has been found that
855 only localized buckling in the inward direction can be triggered before the
856 buckling moment is reached. Furthermore, a comparison between single and
857 double inward probing schemes highlighted that the longerons will most likely
858 not undergo buckling simultaneously and will rather exhibit a sequential for-
859 mation of buckles known as snaking, which was also supported by the classi-
860 cal post-buckling analysis. However, when probing is not done in the middle
861 of the structure, unstable probing sequences were observed and, therefore,
862 an arc-length solver was used. This refined analysis highlighted complex
863 behaviors such as buckles traveling along the structure and multiple equilib-
864 rium paths juxtaposed next to each other. It has been shown that unstable
865 outward probing can lead to local inward buckling through an interaction
866 between structural components.

867 A particular feature of the equilibrium paths obtained in the present
868 study, which had not been reported before, is the formation of formation of
869 spiral paths that indicate the existence of multiple equilibrium configurations.

870 This generalized probing approach has enabled the construction of a crit-
871 ical probe work map from which we concluded that a single inward buckle
872 forming on a single longeron is the buckling mechanism requiring the least
873 amount of disturbance to be triggered before reaching the buckling moment.
874 An in depth study of the critical buckling mode has enabled the construction
875 of a stability landscape of shell buckling. It highlights the region of stability
876 for the buckled structure as well as the region for which restabilization oc-
877 curs, between the minimal buckling moment and the snaking moment. This
878 stability landscape is qualitatively similar to previous, experimentally based,

879 landscapes for cylindrical shells.

880 Although the core of the paper has presented results for moment-controlled
881 loading, for which probing occurs under a constant moment, rotation-controlled
882 loading has also been studied. It leads to the same qualitative results for this
883 structure, as shown in Appendix A.

884 More generally, it has been shown that the probing methodology can
885 be applied to more complex structures than cylindrical and spherical shells.
886 Therefore, the use of such a technique for complex assemblies of thin-shell
887 components seems to be possible and could enable an in-depth understanding
888 of any structure's buckling sensitivity. One could think about designing for a
889 specific level of disturbance during operations and thus push the structure's
890 capabilities to its fullest. If one does not have a full knowledge of potential
891 disturbances, an experimental determination of the minimal buckling load
892 seems to provide an excellent buckling criterion. However, more work needs
893 to be done to assess how initial imperfections erode the critical probe work
894 required to trigger buckling and how they could provide connections between
895 the adjacent post-buckling path and the fundamental path. Recent studies
896 have suggested that the minimal buckling load varies rather slowly for imper-
897 fections of limited amplitude (about 50 % of the shell thickness) (Royer and
898 Pellegrino, 2020), whereas the critical probe work is significantly affected. A
899 detailed investigation of the role of imperfections on the buckling sensitivity
900 will be the subject of a future paper.

901 **Acknowledgments**

902 FR and SP gratefully acknowledge financial support from the Space Solar
903 Power Project at Caltech.

904 **References**

905 A. Abbasi, D. Yan and P. M. Reis, Probing the buckling of pressurized spher-
906 ical shells, *Journal of the Mechanics and Physics of Solids*, 155 (2021),
907 104545. doi:10.1016/j.jmps.2021.104545.

908 A. Abramian, E. Viroto, E. Lozano, S. M. Rubinstein and T. M. Schnei-
909 der, Nondestructive prediction of the buckling load of imper-
910 fect shells, *Physics Review Letters*, 125 (2020), 22, 225504,
911 doi:10.1103/PhysRevLett.125.225504.

912 M. Arya, N. Lee, S. Pellegrino, Ultralight structures for space solar
913 power satellites, 3rd AIAA Spacecraft Structures Conference, 2016.
914 doi:10.2514/6.2016-1950.

915 B. Audoly, J. W. Hutchinson, Localization in spherical shell buckling,
916 *Journal of the Mechanics and Physics of Solids* 136 (2020) 103720.
917 doi:10.1016/j.jmps.2019.103720.

918 L. H. Donnell, C. C. Wan, Effect of imperfections on buckling of thin cylinders
919 and columns under axial compression., *Journal of Applied Mechanics* 17
920 (1950) 73–83.

- 921 E. Gdoutos, C. Leclerc, F. Royer, D. A. Türk, S. Pellegrino, Ultra-
922 light spacecraft structure prototype, AIAA Scitech 2019 Forum, 2019.
923 doi:10.2514/6.2019-1749.
- 924 E. Gdoutos, A. Truong, A. Pedivellano, F. Royer, S. Pellegrino, Ultralight
925 deployable space structure prototype, AIAA Scitech 2020 Forum, 2020.
926 doi:10.2514/6.2020-0692.
- 927 S. Gerasimidis, E. Virost, J. W. Hutchinson, S. M. Rubinstein, On establishing
928 buckling knockdowns for imperfection-sensitive shell structures, *Journal*
929 *of Applied Mechanics* 85 (2018). doi:10.1115/1.4040455.
- 930 A. Goel, N. Lee, S. Pellegrino, Trajectory design of formation flying con-
931 stellations for space-based solar power, 2017 IEEE Aerospace Conference,
932 2017, pp. 1–11. doi:10.1109/AERO.2017.7943711.
- 933 R. Groh, D. Avitabile, A. Pirrera, Generalised path-following for well-
934 behaved nonlinear structures, *Computer Methods in Applied Mechanics*
935 *and Engineering* 331 (2018) 394 – 426. doi:10.1016/j.cma.2017.12.001.
- 936 R. M. J. Groh, A. Pirrera, On the role of localizations in buckling
937 of axially compressed cylinders, *Proceedings of the Royal Society A:*
938 *Mathematical, Physical and Engineering Sciences* 475 (2019) 20190006.
939 doi:10.1098/rspa.2019.0006.
- 940 M. Hilburger, Developing the next generation shell buckling design factors
941 and technologies, 53rd AIAA/ASME/ASCE/AHS/ASC Structures, Struc-
942 tural Dynamics and Materials Conference. (2012). doi:10.2514/6.2012-
943 1686.

- 944 J. Horák, G. J. Lord, M. A. Peletier, Cylinder buckling: The mountain pass
945 as an organizing center, *SIAM Journal on Applied Mathematics* 66 (2006)
946 1793–1824. doi:10.1137/050635778.
- 947 N. Hu, R. Burgueño, Buckling-induced smart applications: recent ad-
948 vances and trends, *Smart Materials and Structures* 24 (2015) 063001.
949 doi:10.1088/0964-1726/24/6/063001.
- 950 G. Hunt, E. Neto, Localized buckling in long axially-loaded cylindrical
951 shells, *Journal of the Mechanics and Physics of Solids* 39 (1991) 881 –
952 894. doi:https://doi.org/10.1016/0022-5096(91)90010-L.
- 953 J. W. Hutchinson, Buckling of spherical shells revisited, *Proceedings of the*
954 *Royal Society A: Mathematical, Physical and Engineering Sciences* 472
955 (2016) 20160577. doi:10.1098/rspa.2016.0577.
- 956 J. W. Hutchinson, J. M. T. Thompson, Nonlinear buckling behaviour of
957 spherical shells: barriers and symmetry-breaking dimples, *Philosophical*
958 *Transactions of the Royal Society A: Mathematical, Physical and Engi-*
959 *neering Sciences* 375 (2017) 20160154. doi:10.1098/rsta.2016.0154.
- 960 J. W. Hutchinson, J. M. T. Thompson, Nonlinear buckling interaction for
961 spherical shells subject to pressure and probing forces, *Journal of Applied*
962 *Mechanics* 84 (2017). doi:10.1115/1.4036355.
- 963 W. T. Koiter, *On the Stability of Elastic Equilibrium.*, H. J. Paris, Amster-
964 dam, Holland., 1945, pp. 201–213.
- 965 T. Kreilos, T. M. Schneider, Fully localized post-buckling states of cylin-
966 drical shells under axial compression, *Proceedings of the Royal Society*

967 A: Mathematical, Physical and Engineering Sciences 473 (2017) 20170177.
968 doi:10.1098/rspa.2017.0177.

969 C. Leclerc, S Pellegrino, Nonlinear elastic buckling of ultra-thin coilable
970 booms, *International Journal of Solids and Structures*, 203 (2020), 46-56.
971 doi:10.1016/j.ijsolstr.2020.06.042.

972 A. Lee, F. López Jiménez, J. Marthelot, J. W. Hutchinson, P. M. Reis, The
973 geometric role of precisely engineered imperfections on the critical buckling
974 load of spherical elastic shells, *Journal of Applied Mechanics* 83 (2016).
975 doi:10.1115/1.4034431.

976 J. Marthelot, F. López Jiménez, A. Lee, J. W. Hutchinson, P. M. Reis,
977 Buckling of a pressurized hemispherical shell subjected to a probing force,
978 *Journal of Applied Mechanics* 84 (2017). doi:10.1115/1.4038063.

979 E. Medina, P. E. Farrell, K. Bertoldi, C. H. Rycroft, Navigating the land-
980 scape of nonlinear mechanical metamaterials for advanced programmabil-
981 ity, *Phys. Rev. B* 101 (2020) 064101. doi:10.1103/PhysRevB.101.064101.

982 T. Murphey, J. Banik, Triangular rollable and collapsible boom, U.S. Patent
983 7,895,79, 2011.

984 NASA, Buckling of thin-walled circular cylinders. NASA Space Vehicle De-
985 sign Criteria, NASA SP-8007. (Revised 1968). Technical Report, NASA,
986 1965.

987 T. Rahman, E. Jansen, Finite element based coupled mode initial post-
988 buckling analysis of a composite cylindrical shell, *Thin-Walled Structures*
989 48 (2010) 25 – 32. doi:10.1016/j.tws.2009.08.003.

- 990 E. Riks, An incremental approach to the solution of snapping and buckling
991 problems, *International Journal of Solids and Structures* 15 (1979) 529–
992 551. doi:10.1016/0020-7683(79)90081-7.
- 993 F. Royer, Probing the Buckling of Thin-Shell Space Structures, PhD Disserta-
994 tion, California Institute of Technology (2021). doi:10.7907/ksn2-t598.
- 995 F. Royer, S. Pellegrino, Buckling of ultralight ladder-type coilable space
996 structures, *AIAA Scitech 2020 Forum*, 2020. doi:10.2514/6.2020-1437.
- 997 F. Royer, S. Pellegrino, Probing the stability of ladder-type coilable space
998 structures, *AIAA Journal*, 60 (2022), 4, 2000-2012, doi:10.2514/1.J060820.
- 999 J. Shen, R. M. J. Groh, M. Schenk, A. Pirrera, Experimental path-following
1000 of equilibria using Newton’s method. Part I: Theory, modelling, exper-
1001 iments, *International Journal of Solids and Structures*, 210-211 (2021),
1002 203-223, doi:10.1016/j.ijsolstr.2020.11.037.
- 1003 J. Shen, R. M. J. Groh, M. Schenk, A. Pirrera, Experimental path-following
1004 of equilibria using Newton’s method. Part II: Applications and out-
1005 look, *International Journal of Solids and Structures*, 213 (2021), 25-40,
1006 doi:10.1016/j.ijsolstr.2020.11.038.
- 1007 J. Shen, R. M. J. Groh, M. A. Wadee, M. Schenk, A. Pirrera, Prob-
1008 ing the stability landscape of prestressed stayed columns suscepti-
1009 ble to mode interaction, *Engineering Structures*, 251 (2022), 113465,
1010 doi:10.1016/j.engstruct.2021.113465.

- 1011 J. M. T. Thompson, Advances in shell buckling: Theory and experi-
1012 ments, *International Journal of Bifurcation and Chaos* 25 (2015) 1530001.
1013 doi:10.1142/S0218127415300013.
- 1014 J. M. T. Thompson, G. H. M. van der Heijden, Quantified "shock-sensitivity"
1015 above the maxwell load, *International Journal of Bifurcation and Chaos*
1016 24 (2014) 1430009. doi:10.1142/S0218127414300092.
- 1017 J. M. T. Thompson, J. Sieber, Shock-sensitivity in shell-like structures: With
1018 simulations of spherical shell buckling, *International Journal of Bifurcation*
1019 *and Chaos* 26 (2016) 1630003. doi:10.1142/S0218127416300032.
- 1020 J. M. T. Thompson, J. W. Hutchinson, J. Sieber, Probing shells
1021 against buckling: A nondestructive technique for laboratory testing,
1022 *International Journal of Bifurcation and Chaos* 27 (2017) 1730048.
1023 doi:10.1142/S0218127417300488.
- 1024 J. Thompson, L. Virgin, Spatial chaos and localization phenomena
1025 in nonlinear elasticity, *Physics Letters A* 126 (1988) 491 – 496.
1026 doi:[https://doi.org/10.1016/0375-9601\(88\)90045-X](https://doi.org/10.1016/0375-9601(88)90045-X).
- 1027 E. Viot, T. Kreilos, T. M. Schneider, S. M. Rubinstein, Stability
1028 landscape of shell buckling, *Phys. Rev. Lett.* 119 (2017) 224101.
1029 doi:10.1103/PhysRevLett.119.224101.
- 1030 T. Von Karman, H.-S. Tsien, The buckling of thin cylindrical shells under
1031 axial compression, *Journal of the Aeronautical Sciences* 8 (1941) 303–312.
1032 doi:10.2514/8.10722.

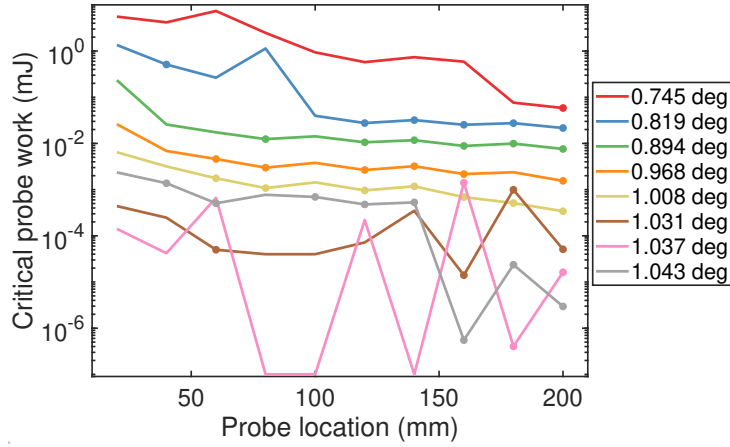
- 1033 M. K. Wadee, G. W. Hunt, A. I. M. Whiting, Asymptotic and Rayleigh-
1034 Ritz routes to localized buckling solutions in an elastic instability prob-
1035 lem, Proceedings of the Royal Society of London. Series A: Math-
1036 ematical, Physical and Engineering Sciences 453 (1997) 2085–2107.
1037 doi:10.1098/rspa.1997.0112.
- 1038 K. K. Yadav, N. L. Cuccia, E. Viot, S. S. Rubinstein and S. Gerasimidis,
1039 A nondestructive technique for the evaluation of thin cylindrical shells’
1040 axial buckling capacity, Journal of Applied Mechanics, 88 (2021), 5,
1041 doi:10.1115/1.4049806.
- 1042 A. Zareei, B. Deng, K. Bertoldi, Harnessing transition waves to realize de-
1043 ployable structures, Proceedings of the National Academy of Sciences 117
1044 (2020) 4015–4020. doi:10.1073/pnas.1917887117.

1045 **Appendix A. Rotation-Controlled Study**

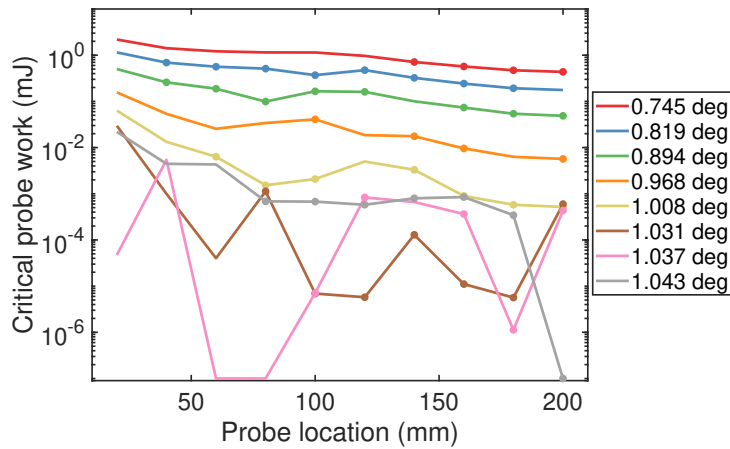
1046 The analysis presented in the paper has been repeated for rotation-controlled
1047 main loading. Here the rotation is prescribed at the two ends of the strips, at
1048 the reference points shown in Figure 2. The moment-controlled and rotation-
1049 controlled studies lead to the same qualitative results. The same buckling
1050 modes and unstable probing paths are observed, and the critical probe work
1051 maps can be computed. These maps are shown in Figure A.19a for the single
1052 inward probing scheme and in Figure A.19b for the single outward probing
1053 scheme. The values of applied rotations are chosen such that they corre-
1054 spond one-to-one to the moment magnitudes in Figure 17, on the structure’s
1055 fundamental path.

1056 One important difference here is that the probe work accounts for all the
1057 external work since the end moments are not doing any work. For rota-
1058 tions (or corresponding moments) between 0.745 deg and 0.894 deg, a higher
1059 critical probe work is required to trigger snap-buckling when the loading is
1060 rotation-controlled rather than moment-controlled. In this initial range of
1061 rotations, the minimum critical probe work is still achieved by probing in
1062 the center ($z = 200$ mm), and therefore the single inward buckling in the
1063 middle of one longeron is also the critical buckling mechanism for a rotation-
1064 controlled loading. For higher values of rotation, the critical probe work is
1065 higher for the moment-controlled case, even if it has a similar order of mag-
1066 nitude for both types of loading. Closer to the buckling point, we observe
1067 that the critical probe work becomes chaotic across the structure’s length.

1068 For the critical buckling mechanism identified above (single inward buckle
1069 at $z = 200$ mm), the rotation-controlled stability landscape can be built



(a)



(b)

Figure A.19: (a) Critical probe work map for single inward probing scheme. Dots denote solutions corresponding to the first zero value of the probe force, corresponding to a buckled equilibrium. (b) Critical probe work map for single outward probing scheme.

1070 and is shown in Figure A.20. It presents the same features as the moment-
 1071 controlled stability landscape. In both studies, the probing path restabilizes
 1072 after the minimally buckled state. The minimal buckling rotation is about
 1073 70% of the classical buckling rotation which is comparable to the minimal

1074 buckling moment which was 68% of the classical buckling moment. Probing
 1075 becomes unstable close to the snaking point which explains the missing area
 1076 in the map shown in Figure A.20. It is important to point out that when the
 1077 applied rotation is held constant, the area under the probe force vs. probe
 1078 displacement curve is the critical probe work but also the energy barrier
 1079 between the unbuckled equilibrium and the unstable buckled equilibrium.

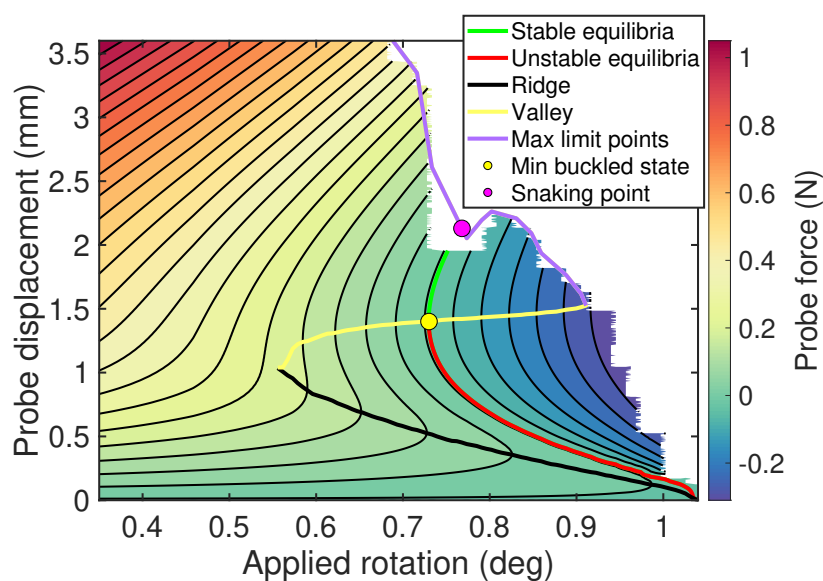


Figure A.20: Stability landscape for critical buckling mechanism (single inward buckling in the middle), and for rotation-controlled loading.